UNIVERSITÀ DI PARMA

Dottorato di Ricerca in Tecnologie dell'Informazione

XXX Ciclo

ADVANCED TRANSCEIVERS FOR SATELLITE COMMUNICATIONS

Coordinatore:

Chiar.mo Prof. Marco Locatelli

Tutor:

Chiar.mo Prof. Giulio Colavolpe

Dottorando: *Michelangelo Ricciulli*

Anni 2014/2017

A mia madre

Table of Contents

List of Figures

List of Tables

List of Acronyms

ACM Adaptive Coding and Modulation.

AIR Achievable Information Rate.

APSK Amplitude-Phase Shift Keying.

ASE Achievable Spectral Efficiency.

AWGN Additive White Gaussian Noise.

BCJR Bahl, Cocke, Jelinek and Raviv.

BICM Bit Interleaved Coded Modulation.

CRC Cyclic Redundancy Code.

CS Channel Shortening.

DFT Discrete Fourier Transform.

DPD Data PreDistorter.

FDM Frequency Division Multiplexing.

FFT Fast Fourier Transform.

FS Fractionally Spaced.

HPA High Power Amplifier.

IBO Input Back-Off.

IC Interference Cancellation.

ICI Inter-Channel Interference.

IMUX Input Multiplexer.

IoT Internet of Things.

ISI Inter-Symbol Interference.

LAN Local Area Network.

LDPC Low-Density Parity Check.

LEO Low Earth Orbit.

LLR Log Likelihood Ratio.

LPWAN Low Power-Wide Area Network.

LS Least Squares.

MAP Maximum A Posteriori.

MCRLB Modified Cramér-Rao Lower Bound.

MMSE Minimum Mean Square Error.

MODCOD Modulation/Coding.

MSE Mean Square Error.

MSEE Mean Square Estimation Error.

MUD Multiuser Detector.

OMUX Output Multiplexer.

PDF Probability Density Function.

PER Packet Error Rate.

PMF Probability Mass Function.

PSD Power Spectral Density.

PSK Phase Shift Keying.

QAM Quadrature Amplitude Modulation.

RF Radio Frequency.

RLS Recursive Least Squares.

RRC Root Raised Cosine.

SER Symbol Error Rate.

SIMO Single Input-Multiple Output.

SNR Signal-to-Noise Ratio.

SPD Signal PreDistorter.

SUD Single User Detector.

TDM Time Division Multiplexing.

TDMA Time Division Multiple Access.

TFP Time-Frequency Packing.

Introduction

Nowadays everything is becoming connected. It is estimated that by the year 2020 more than 200 billions of devices will be connected all around the world. This exponential growth requires continuous improvements and more efficient use of the resources for each connection of this huge and complex network.

The focus of this thesis will be on satellite communications. They comprehend many applications such as high-quality television services, internet connectivity, telemetry, extension of terrestrial networks and many others. Here, after a short overview of information theoretic results given in Chapter 1, we will focus on improvements in reliability, efficiency, and coverage in three different scenarios of satellite communications. Each scenario will be covered in a different Chapter, where we show the design of new schemes for transmitters and receivers and analyze their performance.

Broadcast and unicast satellite connections probably represent the most popular scenarios in satellite communications. The information source is on the ground and transmits to a satellite transponder, whose main function is to filter out adjacent channels, amplify the signal and re-transmit it to the ground towards the receiver. In broadcast connections, many receivers will get the same signal (e.g, for television services) while unicast connections are mostly used for Internet coverage in remote areas. Chapter 2 proposes a solution that could improve speed or reliability in these scenarios. It is based on the idea that two (or more) neighbor users could cooperate using a side-channel to exchange information about the received signals and thus, collaboratively, implement a diversity receiver. In fact, the increasing demand for high-speed Internet services and high-definition television needs receivers that exploit the channel in the best possible way. Moreover, in these days, the widespread wired and wireless Local Area Network (LAN) could be employed in this context as side-channels. The work is based on the extension of the second generation digital video broadcasting DVB-S2X [1]. Different possible schemes are derived and analyzed. To make it more realistic, we used the hypothesis that the side-channel has not an infinite capacity but it is constrained to a maximum fixed information rate that could pass through it.

Another important scenario in the field of satellite communications is represented by telemetry. Telemetry means measuring using remote devices, and typical applications are represented by Earth observation and collection of environmental data from satellites. In these scenarios, information is thus generated directly on board of satellites and then is sent to the ground. In Chapter 3, we carry out an analysis to find a suitable scheme for both transmitters and receivers meant for these applications. We propose the use of a signal predistorter between the modulator and the High Power Amplifier (HPA) to better compensate the effects of amplifier's non-linearity. Then, we describe improvements in spectral efficiency through optimization of the transmission parameters on board of the satellite and discuss on the benefits of advanced low-complexity receivers.

Internet of Things (IoT) will be among the main contributors to the extreme growth in the number of connected devices. Different transmission schemes and protocols are used in this context and thus gateways are needed to connect the devices to the Internet. However, their diffusion showed the necessity to extend coverage in remote areas (e.g., to collect data from wildlife or pipeline sensors). Chapter 4 describes a way to use a swarm of Low Earth Orbit (LEO) satellites to help in these scenarios, by relaying the messages intended for the gateway when the devices are located far from the urban environments. To remain in the low-orbit (around 700 km above the ground), satellites must maintain a very high speed ($\sim$ 7.5 km/s). Thus, Doppler effect is very strong and can be detrimental for a simple transmission scheme that is not meant to be used on LEO satellites. The study is based on a promising proprietary IoT protocol called *LoRa*, designed to be used in terrestrial communications. The modulation scheme at the physical layer is also proprietary [2] and is slightly different from the traditional modulations found in digital communications textbooks. We will describe this spread-spectrum modulation format, its main properties and we will propose a receiver scheme that could allow the reception of LoRa signals even in this challenging scenario. The results presented in Chapter 4 do not take into account effects of interference coming from all the different users transmitting in the satellite's field of view. However, the interested reader could find details on this discussion in [3].

Chapter 1

Theoretical background

Before the detailed description of the analyzed scenarios and proposed techniques, we present a brief but useful overview of the theoretical background to the results presented in the following chapters. The underlying concepts are taken from *information theory*. Here we introduce Achievable Information Rate (AIR) and Achievable Spectral Efficiency (ASE) and explain why they are important metrics to measure the performance of a communication system. We also introduce the *mismatched detection* and the Channel Shortening (CS) framework. Moreover we show how they can be useful on a satellite scenario.

1.1 Information rate and mismatched detection

Information theory gives us results about the fundamental limits of communications and processing. The building blocks of this subject can be found in [4]. Let us introduce the concept of information rate. If we call $\mathbf{x}$ a vector of transmitted N symbols belonging to a finite alphabet and $\mathbf{y}$ a vector of the same length representing the received symbols, i.e. the symbols passed through the channel, we can define the AIR as

$$I(\mathbf{x};\mathbf{y}) = \lim_{N\to\infty} \frac{1}{N} \mathbb{E}\left[\log_2 \frac{p(\mathbf{y}|\mathbf{x})}{\sum_{\mathbf{x}'} p(\mathbf{y}|\mathbf{x}')P(\mathbf{x}'))}\right] \quad \text{[bits / ch.use]}. \tag{1.1}$$

The operator $\mathbb{E}[\cdot]$ represents the expectation operator, $P(\mathbf{x})$ is the Probability Mass Function (PMF) of the channel inputs and $p(\mathbf{y}|\mathbf{x})$ is the Probability Density Function (PDF) that describes the channel. Thus the AIR is linked both to the choice of the transmitted symbols through the PMF $p(\mathbf{x})$ and to the channel through the PDF $p(\mathbf{y}|\mathbf{x})$. It can be interpreted as the average mutual information per transmitted symbol and thus represents the maximum amount of information bits per each transmitted symbol that can be reliably sent on the channel with the selected input alphabet.

Let us consider a simple channel described by the following equation,

$$\mathbf{y} = \mathbf{H}\mathbf{x} + \mathbf{w}, \tag{1.2}$$

where $\mathbf{H}$ is a Toeplitz matrix representing the Inter-Symbol Interference (ISI) introduced by the channel and $\mathbf{w}$ is a vector whose elements are complex Additive White Gaussian Noise (AWGN) samples, with mean zero and variance N_0.

Computing the AIR in closed form through (1.1) is not a straightforward operation. However, using the Monte Carlo method described in [5], we can compute the AIR numerically since we have available the optimal Maximum A Posteriori (MAP) symbol detector for this kind of channel. This optimal detector is based on the Bahl, Cocke, Jelinek and Raviv (BCJR) algorithm [6]. The BCJR will be based on the channel PDF,

$$\begin{aligned} p(\mathbf{y}|\mathbf{x}) &= \frac{1}{(\pi N_0)^N} \exp\left(-\frac{\|\mathbf{y}-\mathbf{H}\mathbf{x}\|^2}{N_0}\right) \\ &= \frac{1}{(\pi N_0)^N} \exp\left(-\frac{\mathbf{y}^\dagger\mathbf{y} - 2\Re\left\{\mathbf{y}^\dagger\mathbf{H}\mathbf{x}\right\} + \mathbf{x}^\dagger\mathbf{G}\mathbf{x}}{N_0}\right), \end{aligned} \tag{1.3}$$

where we introduced the matrix $\mathbf{G} = \mathbf{H}^\dagger\mathbf{H}$. However, the feasibility of the MAP detector depends on the length L of the memory introduced by the channel through the matrix $\mathbf{H}$. In fact, calling M the cardinality of the alphabet, the BCJR detector's complexity is $O\left(M^L\right)$ or, in other words, it depends exponentially on L. Moreover, we cannot always fully describe the channel in the simple form of (1.2). For the sake of example, the satellite channel typically includes a nonlinear transponder.

We can now introduce the mismatched detection principle described in [7]. In fact, we can think of an auxiliary channel described by the PDF $q(\mathbf{y}|\mathbf{x})$ for which an optimal detector is feasible. Then, we can compute through the algorithm [5] the quantity,

$$I_q(\mathbf{x};\mathbf{y}) = \lim_{N\to\infty} \frac{1}{N}\mathbb{E}\left[\log_2 \frac{q(\mathbf{y}|\mathbf{x})}{\sum_{\mathbf{x}'} q(\mathbf{y}|\mathbf{x}')P(\mathbf{x}'))}\right] \quad . \tag{1.4}$$

This will be computed using the output $\mathbf{y}$ of the actual channel but employing a detector based on the auxiliary channel PDF $q(\mathbf{y}|\mathbf{x})$. As demonstrated in [7], $I_q(\mathbf{x};\mathbf{y})$ will be a lower bound to $I(\mathbf{x};\mathbf{y})$, but it will be also achievable by that detector. This means that we are capable of numerically compute the AIR that will depend on the input constellation, on the channel, and the detector based on $q(\mathbf{y}|\mathbf{x})$. The detector will be thus optimal for the auxiliary channel but sub-optimal for the actual channel. The next step will be understanding how to properly choose the auxiliary channel through the CS technique.

1.2 Channel Shortening

To design a receiver with a reasonable complexity, many approaches have been proposed. We can think of two basic types of algorithms: one that selects only a fraction of the trellis to explore (see [8], [9] and [10]) and the other that builds a reduced trellis to be fully explored (e.g., [11]). We describe here the Channel Shortening technique proposed in [12], that belongs to the second kind of algorithms. It is based on the channel model (1.2) and, even though it is designed under the hypothesis of Gaussian inputs $\mathbf{x}$, it works also on finite cardinality alphabets.

The first step consists of choosing the memory of the reduced complexity detector $\nu \leq L$. Then, the algorithm computes the matrices $\mathbf{H}_r$ and $\mathbf{G}_r$ to be used in the mismatched detector based on the following auxiliary channel model

$$q(\mathbf{y}|\mathbf{x}) \propto \exp\left(-\mathbf{y}^\dagger\mathbf{y} - 2\Re\left\{\mathbf{y}^\dagger\mathbf{H}^r\mathbf{x}\right\} + \mathbf{x}^\dagger\mathbf{G}^r\mathbf{x}\right) .$$

The computation of $\mathbf{H}^r$ and $\mathbf{G}^r$ is the result of a maximization of a lower bound to the information rate, differently from other works on the subject that performed an optimization of the Minimum Mean Square Error (MMSE) [11]. The elements of the

$\mathbf{G}^r$ matrix must satisfy the constraint $\{\mathbf{G}^r{}_{mn}\} = 0$ for $|m-n| > \nu$. For ISI channels $\mathbf{G}^r$ and $\mathbf{H}^r$ are Toeplitz matrices completely characterized by the discrete-time sequences g_k^r e h_k^r. Let us call $G^r(\omega)$ and $H^r(\omega)$ the Fourier transform of those sequences. Then, we can compute

$$H^r(\omega) = \frac{H^*(\omega)}{|H(\omega)|^2 + N_0}(G_r(\omega)+1).$$

and $G^r(\omega)$ can be found through the following factorization,

$$\mathbf{G}_r + \mathbf{I} = \mathbf{U}\mathbf{U}^\dagger$$

where $\mathbf{U}$ is an upper triangular matrix. Defining,

$$A(\omega) = \frac{N_0}{|H(\omega)|^2 + N_0} \tag{1.5}$$

and its inverse Fourier transform a_k, we can build the Toeplitz matrix

$$\tilde{\mathbf{A}}^\nu = \begin{bmatrix} a_0 & \cdots & a_{\nu-1} \\ \vdots & \ddots & \vdots \\ a_{-(\nu-1)} & \cdots & a_0 \end{bmatrix}.$$

and the vector $\mathbf{a}^\nu = [a_1 \cdots a_\nu]$. It can be shown that the elements of matrix $\mathbf{U}$ can be obtained through the following equations

$$u_0 = \frac{1}{\sqrt{a_0 - \mathbf{a}^\nu(\tilde{\mathbf{A}}^\nu)^{-1}\mathbf{a}^\dagger}}$$

$$\mathbf{u}^\nu = \left[u_0, -u_0\mathbf{a}^\nu(\tilde{\mathbf{A}}^\nu)^{-1}\right].$$

CS is a very general framework and it is possible to demonstrate that for the simplest case of $\nu = 0$ it collapses into an unbiased version of MMSE receiver, while it represents the optimal detector for $\nu = L$. In [13] and [14], the CS has been extended to receivers that perform iterative detection and decoding. At each iteration, the filters are updated based on the quality of the soft-decision and the soft-symbols are employed to perform an Interference Cancellation (IC). In this IC-CS the soft-symbols are filtered by a filter $R(\omega)$ and subtracted to the received samples. $R(\omega)$ can be found through an iterative algorithm, since no closed-form solution can be found for it.

Both these reduced complexity receivers need to know the channel matrix $\mathbf{H}$. The work performed in [15], instead, shows a way to implement the first version of CS in an adaptive scenario. It is shown that $A(\omega)$ in (1.5) is just the Power Spectral Density (PSD) of the MMSE sequence $e_k = y_{\mathrm{MMSE}k} - x_k$, where $\{y_{\mathrm{MMSE}_k}\}$ are the received samples after an MMSE filter. It also shows that introducing the MMSE filter $H_{\mathrm{MMSE}}(\omega)$, $H^r(\omega)$ can be factorized as,

$$H^r(\omega) = H_{\mathrm{MMSE}}(\omega)(G_r(\omega)+1).$$

So the CS receiver could be employed after an adaptive MMSE filter. This can be computed trough a Least Squares (LS) or Recursive Least Squares (RLS) algorithm [16]. Then, by the error sequence e_k we can compute $\tilde{\mathbf{A}}^\nu$ and $\mathbf{a}$ since,

$$\hat{a}_k = \frac{1}{N-k}\sum_{i=0}^{N-k-1} e_{i+k}e_i^*.$$

Similarly, also the IC-CS receiver could be implemented in an adaptive fashion, but with some degrees of approximation. In fact, while the CS needs only the first $\nu+1$ taps of b_k, the IC-CS needs the full PSD $B(\omega)$. So, in a practical implementation, we can use the estimated b_k taking taps until b_k is small enough to be negligible. The adaptive version of the CS is useful on many satellite scenarios since the channel is not given in a simple closed form due to nonlinear distortions coming from the satellite amplifiers. In fact, a nonlinear HPA is present on board of a satellite (see Chapter 2 and Chapter 3).

1.3 Spectral efficiency and Time-Frequency Packing

Even though AIR seems a good metric to judge the amount of information that can be sent through a given channel, it gives no information about how efficiently we are exploiting the channel resources. In fact, we could reach a good performance but maybe using too much of the time and frequency resources. That is why we introduce the ASE, taking into account also the amount of occupied bandwidth W and the symbol period T_s

$$\mathrm{ASE} = \frac{I(\mathbf{x};\mathbf{y})}{W T_\mathrm{s}} \, [\mathrm{bit/s/Hz}] \,. \tag{1.6}$$

This idea leads to the concept of Time-Frequency Packing (TFP) [17]. In fact, if we occupy less bandwidth W (e.g., through tighter filters) and transmit more rapidly (smaller T_s), we are giving up orthogonality and we are introducing some degrees of ISI and Inter-Channel Interference (ICI). This could lead to a smaller AIR but since we are also decreasing the product $W T_\mathrm{s}$, there is a possible efficiency improvement for an appropriate choice of $W T_\mathrm{s}$. Of course, depending on the channel and on the amount of introduced memory, the optimal receiver could quickly become unfeasible. So, we use the achievable lower bound $I_q(\mathbf{x};\mathbf{y})$ instead of the optimal $I(\mathbf{x};\mathbf{y})$ to compute the ASE in (1.6). Also, we employ the CS framework since it optimizes the AIR for a fixed complexity constraint. This technique led to significant improvement in different scenarios like in wireless [18], optical [19], and also satellite links [20].

Chapter 2

Cooperative Receivers Through a Constrained Link

The always increasing demand for high-speed Internet services and high-definition television needs receivers that exploit the channel in the best possible way. Moreover, in these days, both wired and wireless LAN are widespread. In this Chapter, we study, from a physical layer perspective, a scheme where satellite receivers exploit a LAN (just for the sake of an example, but could be any other kind of link), as a way to exchange information and thus, collaboratively, implement a diversity receiver. The standard on which the study is performed is the extension of the second generation digital video broadcasting DVB-S2X [1]. In the ideal case of infinite backhaul capacity, assuming the same channel model but with different noise process realizations, we could achieve a 3 dB gain with just two cooperating receivers. In fact, a simple receiver should only need to average out the noise by coherently summing the two received signals. However, we analyze the performance of a scheme where the capacity of the cooperation link is constrained to a fixed rate per channel use. Thus, one of the receivers needs to suitably compress its signal before sending it to the other user; in this Chapter we assume the simplest possible solution where the helping user is merely quantizing its signal, in order to reduce the complexity burden for the helping user as much as possible. This scheme could also be applied to cooperation among many users.

The application scenarios are multiple. An example could be for broadcasting. Users at the edge of a coverage area could cooperate to have more reliable or improved service. In a unicast scenario for Internet connection, where a Time Division Multiple Access (TDMA) is employed, the users could cooperate by turn: each user, during its idle time-slots, could receive the signal meant for the other and then send the quantized version. Thus, the gains in Signal-to-Noise Ratio (SNR) could be exploited by the Adaptive Coding and Modulation (ACM) scheme to have improved connections.

The idea of taking advantage of a constrained backhaul link has already been proposed and applied to the base stations of a cellular system (see, e.g., [21]). We instead adopt it to synthesize satellite receiver cooperation, where the complexity constraint can be tighter. Moreover, as a performance metric, we take a lower bound to the *information rate* of the cooperative receiver, based on the joint distribution of the full version and the quantized version of the signal, rather than just the information rate of the quantized signal alone. The computation of the information rate will be based on the Monte Carlo method described in [5].

In this chapter, we will first describe the reference receiver, the employed channel model and the assumptions on which our work is based. Then, we will give a description of different approaches for receivers and quantization schemes and we report, and comment upon, the results in terms of mutual information and PER for the different approaches.

2.1 Employed channel models

2.1.1 Reference model

The channel we are studying is the single-carrier per transponder satellite channel, where the DVB-S2X standard is employed. The information bits are generated and encoded in the gateway. The channel coding is the Low-Density Parity Check (LDPC) foreseen by the standard. The bits are then interleaved, mapped to complex symbols and finally sent to a satellite transponder. The complex envelope of the signal output

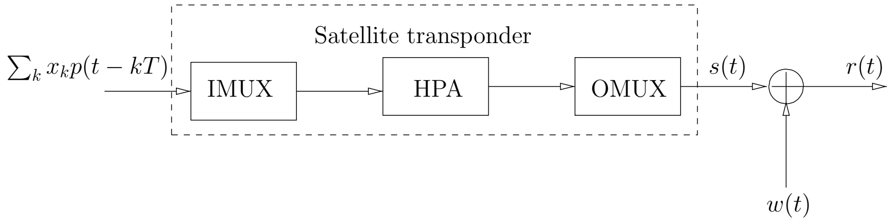

Figure 2.1: Block diagram of the satellite transponder.

from the Earth gateway is thus,

$$x(t) = \sum_k x_k p(t - kT_s).$$

The complex symbols x_k belong to Amplitude-Phase Shift Keying (APSK) constellations, as defined in the DVB-S2X standard [1, 22], while T_s is the symbol interval, $p(t)$ a Root Raised Cosine (RRC) pulse with roll-off factor β and signal bandwidth $W = (1+\beta)/T$. The values of β and W have been chosen according to the optimization performed in [23], and thus set to $\beta = 0.05$ and a baud rate $R_s = \frac{1}{T} = 37$ Mbaud.

The transponder is composed of an Input Multiplexer (IMUX) filter to remove adjacent channel interference, a HPA that introduces non-linear distortions and an Output Multiplexer (OMUX) to reduce the spectral regrowth due to the HPA. The HPA is modeled as a memoryless non-linearity defined by its AM/AM and AM/PM characteristics. The IMUX and OMUX filters have 3 dB bandwidths of $W_{\text{IMUX}} = 42$ MHz and $W_{\text{OMUX}} = 38$ MHz respectively. Their frequency responses are shown in Fig. 2.2 and 2.3 while HPA's AM/AM and AM/PM characteristics can be found in Fig. 2.4 (see also [22]).

We point out that $x(t)$ is modeled as noiseless and noise is taken into account as AWGN between the transponder and the receiver. A block diagram is depicted in Fig. 2.1.

The front-end of the receiver is based on a Fractionally Spaced (FS) MMSE detector [24] with oversampling factor $\eta = 2$. The received signal $r(t)$ is first filtered by a low-pass front-end with a bandwidth sufficiently large to permit the subsequent

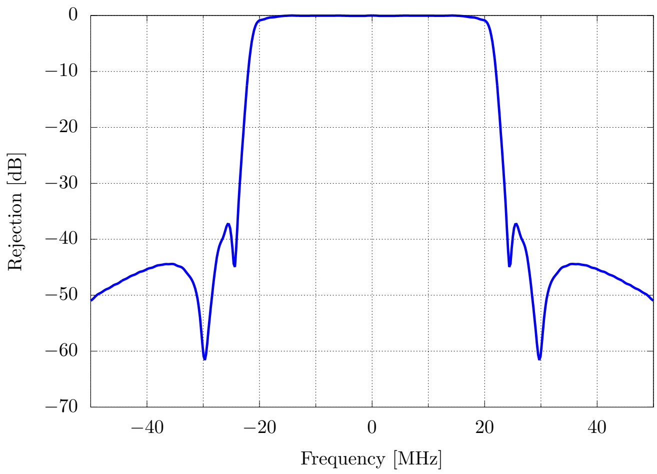

Figure 2.2: IMUX frequency response.

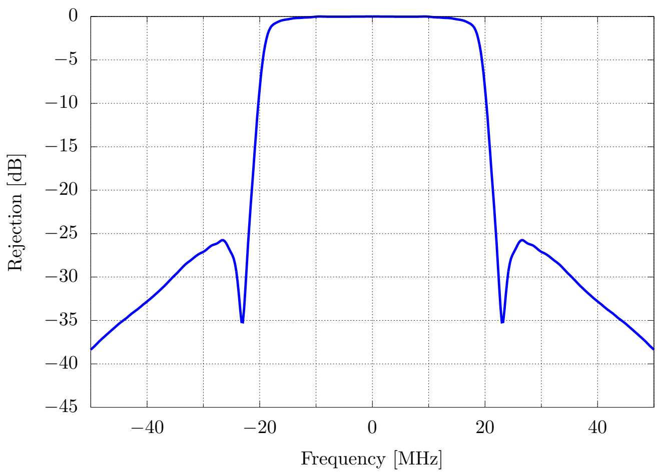

Figure 2.3: OMUX frequency response.

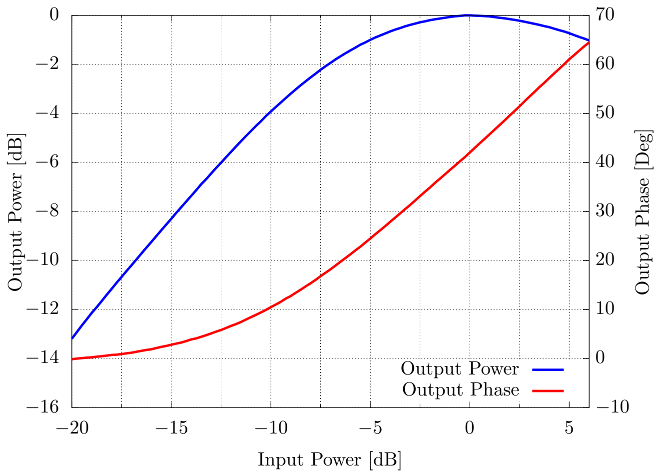

Figure 2.4: HPA AM/AM and AM/PM characteristics.

oversampling at a sampling rate ηR_s [25]. Then, after FS-MMSE filtering and down-sampling, we obtain the samples y_k where k is the symbol time index.

To mitigate the effects of HPA non-linearity, a memoryless Data PreDistorter (DPD) [26] is used at the transmitter, together with a certain amount of Input Back-Off (IBO) which depends on the cardinality of the constellation [27]. We also point out that perfect synchronization at the receiver is assumed.

Within satellite communications, it is customary to define the SNR as P_{sat}/N, where P_{sat} is the saturation power of the HPA, while N is the noise power over the OMUX bandwidth. This is related to E_s/N_0 as,

$$\frac{P_{\text{sat}}}{N} = \frac{E_s}{N_0} \frac{R_s}{W_{\text{OMUX}}} \text{OBO},$$

where OBO stands for the *output back-off* of the HPA.

2.1.2 Cooperation between terminals

We employ a matrix formulation, so that, e.g., the transmitted symbols are represented with the vector $\mathbf{x} = [x_1, \cdots, x_N]^T$ where N is the number of transmitted symbols.

We analyze a scheme with two users that are physically close and can receive, in the absence of noise, the same signal $s_1(t)$. User 2 is helping user 1 through a side-channel with a capacity b_c bits per symbol time. For the sake of simplicity, we consider an error-free side-channel and a negligible delay. See Fig. 2.5 for an overview of the analyzed scenario. We denote by $\mathbf{y}^{(i)} = \left[y_1^{(i)}, \cdots, y_N^{(i)}\right]^T$ the vector containing the digital samples received by user i. The subscript k in $y_k^{(i)}$ is the symbol time index and sampling is done in the same way as in the reference scheme. The channel model is based on the assumption that the signals received by the two users are affected by the same ISI and have the same channel gains, but it is straightforward to extend the model to include different channels. However, our assumption is reasonable whenever the two users are physically close. The channel is represented by an $N \times N$ matrix $\mathbf{H}$. The number of rows and columns should actually be different to take into account the channel tails, but this is irrelevant asymptotically as N grows without bounds and simplifies the notation. The signals are also affected by two independent AWGN processes $\mathbf{n}_1, \mathbf{n}_2 \sim \mathscr{CN}(\mathbf{0}, N_0\mathbf{I})$. Since the side-channel is constrained in capacity to b_c bits per channel use, we need a lossy compression of $\mathbf{y}^{(2)}$ to reduce its entropy. We opted for a quantization of the signal $\mathbf{y}^{(2)}$, where each element $y_k^{(2)}$ is quantized to a set $\mathscr{Q}$ with cardinality $|\mathscr{Q}| = 2^{b_c}$, through a quantizer $q : \mathbb{C} \to \mathscr{Q}$. The quantized version of $\mathbf{y}^{(2)}$ will be represented as $\hat{\mathbf{y}}^{(2)}$. The system as seen by user 1 (i.e., the user that is receiving a quantized version of the same signal, but with another noise realization), can be modeled as a non-linear Single Input-Multiple Output (SIMO)-ISI channel:

$$\begin{bmatrix} \mathbf{y}^{(1)} \\ \hat{\mathbf{y}}^{(2)} \end{bmatrix} = \begin{bmatrix} \mathbf{y}^{(1)} \\ q(\mathbf{y}^{(2)}) \end{bmatrix} = \begin{bmatrix} \mathbf{H}\mathbf{x} + \mathbf{n}_1 \\ q(\mathbf{H}\mathbf{x} + \mathbf{n}_2) \end{bmatrix}.$$

So, we should design a proper scalar quantization function $q(\cdot)$ and a receiver scheme to maximize the mutual information based on the joint distribution of $(\mathbf{y}^{(1)}, \hat{\mathbf{y}}^{(2)})$, namely $I(\mathbf{x}; \mathbf{y}^{(1)}, \hat{\mathbf{y}}^{(2)})$, that can be computed as,

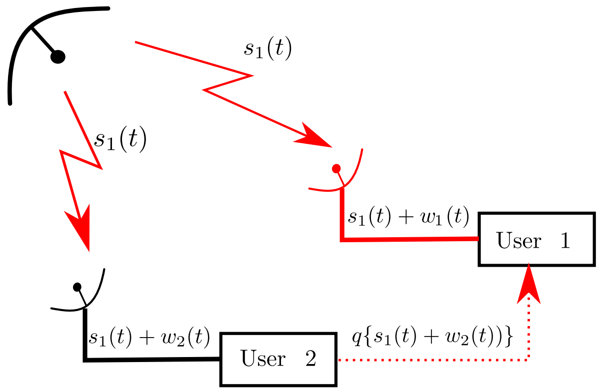

Figure 2.5: Simplified scheme of the analyzed system. The same signal, but with different noise realization, is received by both users. Then user 2 send a quantized version of its signal to user 1 through a constrained link.

$$I(\mathbf{x};\mathbf{y}^{(1)},\hat{\mathbf{y}}^{(2)}) = \lim_{N\to\infty} \frac{\mathbb{E}_{p(\mathbf{y}^{(1)},\hat{\mathbf{y}}^{(2)},\mathbf{x})}\left[\log_2 \frac{p(\mathbf{y}^{(1)},\hat{\mathbf{y}}^{(2)},\mathbf{x})}{p(\mathbf{y}^{(1)},\hat{\mathbf{y}}^{(2)})p(\mathbf{x})}\right]}{N}. \tag{2.1}$$

The information transfer can be represented by the Markov chain $\mathbf{x} \to (\mathbf{y}^{(1)},\mathbf{y}^{(2)}) \to (\mathbf{y}^{(1)},\hat{\mathbf{y}}^{(2)})$. Rate distortion theory [4] could be helpful to find an optimal quantization scheme from an information rate perspective, since it minimizes a certain distortion metric given a target rate. However, the techniques studied in this field are usually working with a quantization of signals not affected by noise. We are instead quantizing the noisy signal $\mathbf{y}^{(2)}$ coming from the noiseless source $\mathbf{x}$. Thus, optimizing the information transfer in $\mathbf{y}^{(2)} \to \hat{\mathbf{y}}^{(2)}$, neglecting that the actual information source is $\mathbf{x}$, is not guaranteed to optimize the whole information transfer $\mathbf{x} \to \mathbf{y}^{(2)} \to \hat{\mathbf{y}}^{(2)}$ [28]. Also, the distortion function is minimizing a distance (typically Euclidean distance) between the quantizer's inputs and outputs but, as we will see in the following sections, the quantization scheme with better gains does not always need to minimize this distance.

We also point out that computation of information rate is not possible in closed form for the satellite channel, and we will thus compute it by the Monte Carlo based algorithm from [5]. So, choosing a proper $q(\cdot)$ and a proper receiver to optimize (1) is a tough problem to treat mathematically in closed form. We will thus try heuristic approaches that make use of low-complexity schemes both for the quantization scheme and the receiver design, to avoid much computational load for this kind of devices.

2.2 Proposed solutions

2.2.1 MMSE approach

The quantized symbols are $\hat{\mathbf{y}}^{(2)} = q\left(\mathbf{y}^{(2)}\right)$. We can model them as,

$$\hat{\mathbf{y}}^{(2)} = \mathbf{y}^{(2)} + \mathbf{n}_2 + \mathbf{n}_q,$$

where $\mathbf{n}_q$ is the noise due to quantization. So the channel seen by user 1 becomes,

$$\mathbf{y} = \begin{bmatrix} \mathbf{y}^{(1)} \\ \hat{\mathbf{y}}^{(2)} \end{bmatrix} = \mathbf{H}_t\mathbf{x} + \begin{bmatrix} \mathbf{n}_1 \\ \mathbf{n}_2 + \mathbf{n}_q \end{bmatrix},$$

where $\mathbf{H}_t = \begin{bmatrix} \mathbf{H} \\ \mathbf{H} \end{bmatrix}$ is a $2N \times N$ block matrix. Both in this and in the following subsection we employ a simple quantization scheme, based on equally spaced symbols belonging to square or non-square Quadrature Amplitude Modulation (QAM), for an even or odd number of quantization bits respectively.

The receiver will be based on an extension of the unbiased linear MMSE receiver [29] for SIMO-ISI channels. Let us introduce $\mathbf{H}_{\text{MMSE}}$, which is an $N \times 2N$ matrix representing the MMSE filter. Then we define $\mathbf{y}_{\text{MMSE}} = \mathbf{H}_{\text{MMSE}}\mathbf{y}$ as the $N \times 1$ vector at the output of the MMSE filter and the MMSE bias α, which can be computed as a function of the Mean Square Error (MSE) $\alpha = 1 - \mathbb{E}\left[|y_{\text{MMSE}k} - x_k|^2\right]$. The unbiased receiver needs to implement a symbol by symbol receiver based on,

$$\hat{x}_k = \arg\min_{x_k} |y_{\text{MMSE}k} - \alpha x_k|^2. \tag{2.2}$$

To deal with the quantization noise, that is not a white Gaussian process and is not guaranteed to be uncorrelated with the information symbols, we keep a more general notation based on *covariance matrices* rather than on channel matrix $\mathbf{H}$ and noise power spectral density N_0. The covariance matrices are defined as,

$$\mathbf{C}_{\mathrm{xy}} = \mathbb{E}\left[(\mathbf{x}-\mathbb{E}[\mathbf{x}])(\mathbf{y}-\mathbb{E}[\mathbf{y}])^{\dagger}\right]$$
$$\mathbf{C}_{\mathrm{yy}} = \mathbb{E}\left[(\mathbf{y}-\mathbb{E}[\mathbf{y}])(\mathbf{y}-\mathbb{E}[\mathbf{y}])^{\dagger}\right].$$

We start computing the MSE matrix, that is needed to compute the bias α. The MSE matrix is,

$$\begin{aligned}\mathbf{A} &= \mathbb{E}\left[(\mathbf{y}_{\mathrm{MMSE}}-\mathbf{x})(\mathbf{y}_{\mathrm{MMSE}}-\mathbf{x})^{\dagger}\right] \\ &= -\mathbf{C}_{\mathrm{xy}}\mathbf{C}_{\mathrm{yy}}^{-1}\mathbf{C}_{\mathrm{xy}}^{\dagger}+\mathbf{I}, \end{aligned} \tag{2.3}$$

where $\mathbf{I}$ is the identity matrix, representing $\mathbf{C}_{\mathrm{xx}}$ under the assumption of unit energy and uncorrelated transmit symbols.

We can now notice how these covariance matrices can be expressed as block matrices of the form,

$$\mathbf{C}_{\mathrm{xy}} = \mathbb{E}\left[\mathbf{x}\mathbf{y}^{\dagger}\right] = \begin{bmatrix} \mathbf{C}_{\mathrm{xy}^{(1)}} & \mathbf{C}_{\mathrm{x}\hat{\mathrm{y}}^{(2)}} \end{bmatrix}$$
$$\mathbf{C}_{\mathrm{yy}} = \mathbb{E}\left[\mathbf{y}\mathbf{y}^{\dagger}\right] = \begin{bmatrix} \mathbf{C}_{\mathrm{y}^{(1)}\mathrm{y}^{(1)}} & \mathbf{C}_{\mathrm{y}^{(1)}\hat{\mathrm{y}}^{(2)}} \\ \mathbf{C}^{\dagger}_{\mathrm{y}^{(1)}\hat{\mathrm{y}}^{(2)}} & \mathbf{C}_{\hat{\mathrm{y}}^{(2)}\hat{\mathrm{y}}^{(2)}} \end{bmatrix},$$

where $\mathbf{C}_{\mathrm{xy}^{(1)}}$, $\mathbf{C}_{\mathrm{x}\hat{\mathrm{y}}^{(2)}}$, $\mathbf{C}_{\mathrm{y}^{(1)}\hat{\mathrm{y}}^{(2)}}$ are square $N \times N$ Toeplitz matrices.

To simplify the notation, we resort to Szegő's Theorem applying spectral decomposition to these block matrices. Asymptotically as $N \to \infty$, we can equivalently work with the Fourier transform of the sequence associated with each Toeplitz matrix. Denoting the $N \times N$ Fourier matrix by $\mathbf{Q}$ and the Fourier transform of a square matrix $\mathbf{C}$ by $\tilde{\mathbf{C}} = \mathbf{Q}^{\dagger}\mathbf{C}\mathbf{Q}$, we can write,

$$\mathbf{L}_{\mathrm{xy}} = \mathbf{Q}^{\dagger}\mathbf{C}_{\mathrm{xy}} \begin{bmatrix} \mathbf{Q} & \mathbf{0} \\ \mathbf{0} & \mathbf{Q} \end{bmatrix} = \begin{bmatrix} \tilde{\mathbf{C}}_{\mathrm{xy}^{(1)}} & \tilde{\mathbf{C}}_{\mathrm{x}\hat{\mathrm{y}}^{(2)}} \end{bmatrix}$$

$$\mathbf{L}_{\mathrm{yy}} = \begin{bmatrix} \mathbf{Q}^{\dagger} & \mathbf{0} \\ \mathbf{0} & \mathbf{Q}^{\dagger} \end{bmatrix} \mathbf{C}_{\mathrm{yy}} \begin{bmatrix} \mathbf{Q} & \mathbf{0} \\ \mathbf{0} & \mathbf{Q} \end{bmatrix} = \begin{bmatrix} \tilde{\mathbf{C}}_{\mathrm{y}^{(1)}\mathrm{y}^{(1)}} & \tilde{\mathbf{C}}_{\mathrm{y}^{(1)}\hat{\mathrm{y}}^{(2)}} \\ \tilde{\mathbf{C}}^{\dagger}_{\mathrm{y}^{(1)}\hat{\mathrm{y}}^{(2)}} & \tilde{\mathbf{C}}_{\hat{\mathrm{y}}^{(2)}\hat{\mathrm{y}}^{(2)}} \end{bmatrix},$$

where all the $\tilde{\mathbf{C}}$ are diagonal matrices and each diagonal is the Fourier transform of a covariance sequence. For the sake of example, $\tilde{\mathbf{C}}_{\mathrm{xy}^{(1)}}$ has as diagonal the Fourier transform function $\tilde{C}_{\mathrm{xy}^{(1)}}(\omega)$, whose inverse-transform is the covariance sequence $\mathbf{c}_{\mathrm{xy}^{(1)}}$ defined by its elements,

$$c_{\mathrm{xy}^{(1)}_k} = \mathbb{E}\left[x_l y^{(1)}_{l+k}\right].$$

We also make use of bold notation (e.g., $\mathbf{L}_{yy}(\omega)$) to describe a matrix of functions depending on the angular frequency ω. In such a way, the diagonal form allows us to carry out the inversion in (2.3) straightforwardly using the block matrix inversion formula,

$$\mathbf{L}^{-1}_{\mathrm{yy}}(\omega) = \frac{\begin{bmatrix} C_{\hat{\mathrm{y}}^{(2)}\hat{\mathrm{y}}^{(2)}}(\omega) & -C_{\mathrm{y}^{(1)}\hat{\mathrm{y}}^{(2)}}(\omega) \\ -C^{\dagger}_{\mathrm{y}^{(1)}\hat{\mathrm{y}}^{(2)}}(\omega) & C_{\mathrm{y}^{(1)}\mathrm{y}^{(1)}}(\omega) \end{bmatrix}}{C_{\mathrm{y}^{(1)}\mathrm{y}^{(1)}}(\omega)C_{\hat{\mathrm{y}}^{(2)}\hat{\mathrm{y}}^{(2)}}(\omega) - |C_{\mathrm{y}^{(1)}\hat{\mathrm{y}}^{(2)}}(\omega)|^2} \tag{2.4}$$

and thus $A(\omega)$, the Fourier transform associated to (2.3), is,

$$\begin{aligned} A(\omega) =& \frac{|C_{\mathrm{xy}^{(1)}}(\omega)|^2 C_{\hat{\mathrm{y}}^{(2)}\hat{\mathrm{y}}^{(2)}}(\omega) + C_{\mathrm{y}^{(1)}\mathrm{y}^{(1)}}(\omega)|C_{\mathrm{x}\hat{\mathrm{y}}^{(2)}}(\omega)|^2}{C_{\mathrm{y}^{(1)}\mathrm{y}^{(1)}}(\omega)C_{\hat{\mathrm{y}}^{(2)}\hat{\mathrm{y}}^{(2)}}(\omega) - |C_{\mathrm{y}^{(1)}\hat{\mathrm{y}}^{(2)}}(\omega)|^2} \\ & - \frac{2\Re\left\{C_{\mathrm{xy}^{(1)}}(\omega)C_{\mathrm{y}^{(1)}\hat{\mathrm{y}}^{(2)}}(\omega)C^{\dagger}_{\mathrm{x}\hat{\mathrm{y}}^{(2)}}(\omega)\right\}}{C_{\mathrm{y}^{(1)}\mathrm{y}^{(1)}}(\omega)C_{\hat{\mathrm{y}}^{(2)}\hat{\mathrm{y}}^{(2)}}(\omega) - |C_{\mathrm{y}^{(1)}\hat{\mathrm{y}}^{(2)}}(\omega)|^2}. \end{aligned} \tag{2.5}$$

We can now call $\mathbf{a}$ the inverse-transform of $A(\omega)$ and express the bias α in (2.2) as,

$$\alpha = 1 - \frac{1}{2\pi}\int_{-\pi}^{\pi} A(\omega)d\omega = 1 - a_0.$$

The MMSE filter is,

$$\mathbf{H}_{\text{MMSE}} = \mathbf{C}_{\text{xy}}\mathbf{C}_{\text{yy}}^{-1} = [\ \mathbf{H}_{\text{MMSE}_1} \quad \mathbf{H}_{\text{MMSE}_2}\ ].$$

Defining the denominator of $A(\omega)$ as a function $D(\omega) = C_{\text{y}^{(1)}\text{y}^{(1)}}(\omega)C_{\hat{\text{y}}^{(2)}\hat{\text{y}}^{(2)}}(\omega) - |C_{\text{y}^{(1)}\hat{\text{y}}^{(2)}}(\omega)|^2$, and by applying the spectral decomposition,

$$\mathbf{H}_{\text{MMSE}}(\omega) = \mathbf{L}_{\text{xy}}(\omega)\mathbf{L}_{\text{yy}}^{-1}(\omega),$$

we can express the MMSE filter in the Fourier domain as,

$$\begin{aligned} H_{\text{MMSE}_1}(\omega) =& \frac{C_{\text{xy}^{(1)}}(\omega)C_{\hat{\text{y}}^{(2)}\hat{\text{y}}^{(2)}}(\omega) - C_{\text{x}\hat{\text{y}}^{(2)}}(\omega)C^{\dagger}_{\text{y}^{(1)}\hat{\text{y}}^{(2)}}(\omega)}{D(\omega)} \\ H_{\text{MMSE}_2}(\omega) =& \frac{C_{\text{x}\hat{\text{y}}^{(2)}}(\omega)C_{\text{y}^{(1)}\text{y}^{(1)}}(\omega) - C_{\text{xy}^{(1)}}(\omega)C_{\text{y}^{(1)}\hat{\text{y}}^{(2)}}(\omega)}{D(\omega)}. \end{aligned}$$

In this form, this receiver is very convenient when we do not have a closed form of the channel because we can simply perform an estimation of the cross and self-covariance sequences. This is the case for the satellite channel and the quantized channel, where the non-linearity comes into play and we need an estimate of their covariance structure. It needs to be pointed out that the unbiased MMSE filtering strategy is very general, since it still applies in case of different channels or different SNRs for user 1 and 2 since only the covariances need to be estimated.

The use of the asymptotic properties of these block matrices simplifies the inversion procedure in (2.4). In fact, instead of computing the inverse of a $2N \times 2N$ matrix, we switched to the simplified case of a 2×2 matrix. Thus, it is also possible to use this algorithm in an extended version. Assuming $U-1$ helping users, we have an $UN \times UN$ matrix to be inverted. After the transformation to the Fourier domain, we obtain a matrix with dimension $U \times U$ where each element is a function of ω, and the inverse could be computed as,

$$\mathbf{C}_{\text{yy}}^{-1}(\omega) = \frac{\text{adj}(\mathbf{C}_{\text{yy}}(\omega))}{\det(\mathbf{C}_{\text{yy}}(\omega))}.$$

Having a closed form of $A(\omega)$ in (2.5) is also useful for channels with a stronger ISI. As explained in Chapter 1, we could easily employ the CS technique since $A(\omega)$ is the only thing needed to compute the CS filter and the reduced trellis. So, this receiver can be easily extended to channels with much more memory, where a BCJR receiver with memory $L > 0$ can give higher performance improvements.

2.2.2 BCJR modifications

The BCJR detector [6] is based on the transition probabilities $p(y_k|x_k, \sigma_k)$, where the state σ_k for an ISI channel with memory L is $\sigma_k = (x_{k-1}, \cdots, x_{k-L})$. In our case, user 1 must base the trellis on $p(y_{1_k}, \hat{y}_{2_k}|x_k, \sigma_k) = p(y_{1_k}|x_k, \sigma_k)p(\hat{y}_{2_k}|x_k, \sigma_k)$, where we exploited the conditional independence of y_{1_k} and $\hat{y}_{2_k}$ given the channel inputs. So, while $p(y_{1_k}|x_k, \sigma_k)$ remains unaltered in the presence of a helping user, we need to accommodate for $p(\hat{y}_{2_k}|x_k, \sigma_k)$, which is very hard to compute in the general case:

$$
\begin{aligned}
p(\hat{y}_{2_k}|x_k, \sigma_k) &= \int_R p(y|x_k, \sigma_k)dy \\
&= \int_R \frac{1}{\pi\sigma^2} \exp\left\{ \frac{|y - \sum_{l=0}^{L} h_l x_{k-l}|^2}{\sigma^2} \right\} dy
\end{aligned}
$$

where $R = \{y \in \mathbb{C} : q(y) = \hat{y}_{2_k}\}$.

If the channel impulse response h_l is real-valued, then it is possible to exploit the independence of the real and complex part to obtain two separate integrals. Moreover, in case of a uniform quantization function, the integrals could be expressed as differences of Q-functions. However, on satellite channels, the above-mentioned simplifications are not exploitable due to the presence of non-linear HPAs. Anyway, regardless of the way $p(\hat{y}_{2_k}|x_k, \sigma_k)$ values are calculated, in a real implementation they can be precomputed and stored in a look-up table. We also point out that this scheme is based on the Forney channel model [30] for the probabilities describing the quantized channel, while a closed form solution based on Ungerboeck model [31] is hard to derive.

In the next section, we resort to a simple estimation of the probabilities $p(\hat{y}_{2_k}|x_k, \sigma_k)$. However, even with a small memory, this estimation process can quickly become prohibitive. If the effects of the channel memory are not too strong, we could thus employ an MMSE filter before quantization. In such a way, the channel state to be taken into account is only one and we can just estimate $p(\hat{y}_{2_k}|x_k)$ without a significant loss in performance. This is applicable to the satellite channel. Even with the signal baud rate optimization as performed in [24, 32], having $R_s = 37$ MBaud, it is possible to see that the introduced memory is negligible. In fact, there is no gain in resorting to a higher memory detector [24].

That being said, this model also remains a valid approximation for any kind of ISI channel and the computed mutual information is achievable since it is an optimal detector for an auxiliary channel [33, 5].

2.2.3 LLR quantization

Since we are interested in the coded performance of the system, one could ask what could be done to focus the information on some bits. The answer is working on quantizations of the bits' Log Likelihood Ratio (LLR). For a given Modulation/Coding (MODCOD) scheme, we could thus focus the information we are sending only on some selected bits of the constellation.

A couple of important remarks are in place. This approach is not guaranteed to be optimal, especially when iterative detection and decoding schemes are performed. It can be, however, optimal when an iterative receiver cannot be employed, as stated by the Bit Interleaved Coded Modulation (BICM) principle [34]. Let us define as $b_{k,i}$ the i^{th} transmitted bit belonging to the k^{th} symbol. Then, we introduce the vector $\mathbf{b} = [b_{1,1} \cdots b_{1,\log_2 M} \cdots b_{N,1} \cdots b_{N,\log_2 M}]^T$ and $\mathbf{b}_i = [b_{0,i} \cdots b_{N,i}]^T$. We point out that i is thus not a temporal index and is $1 \leq i \leq \log_2 M$. We aim at maximizing $C_b = \sum_i I(\mathbf{b}_i; \mathbf{y}^{(1)}, \hat{\mathbf{y}}^{(2)})$, the sum of mutual information between the received signals and the i^{th} bits of each symbol. C_b is an achievable lower bound to $I(\mathbf{x}; \mathbf{y}^{(1)}, \hat{\mathbf{y}}^{(2)})$ since,

$$I(\mathbf{x}; \mathbf{y}^{(1)}, \hat{\mathbf{y}}^{(2)}) = I(\mathbf{b}; \mathbf{y}^{(1)}, \hat{\mathbf{y}}^{(2)}) \geq \sum_i I(\mathbf{b}_i; \mathbf{y}^{(1)}, \hat{\mathbf{y}}^{(2)}),$$

and it is strongly influenced by the bit-mapping function.

We remain with a degree of freedom: the decision on which bits to improve the LLRs of. One could argue that helping the weakest ones first (i.e., the ones with lowest $I(\mathbf{b}_i;\mathbf{y}^{(1)})$ for a given SNR) should be the best approach. Actually, we should decide for the bits with the highest slope $\frac{\partial I(\mathbf{b}_i;\mathbf{y}^{(1)})}{\partial SNR}$. It is thus not guaranteed in the general case that helping the weakest bit first is the best thing to do.

However, we are focusing our attention on high-order modulation schemes for satellite channels. It is easy to argue that for the values of efficiency aimed by these MODCODs, the mutual information will be well above 0 for all values of i. This means that the major constraint for the decoding process will be represented by the weakest bits, since the strongest ones will be near the saturation point of the curve. In Figs. 2.6a, 2.6b, and 2.6c, the values of $I(\mathbf{b}_i;\mathbf{y}^{(1)})$ and $I(\mathbf{x};\mathbf{y}^{(1)})$ are reported for the MODCODs 16, 32, and 64-APSK with a code rate $r_c = 3/4$, $3/4$, and $4/5$, respectively, on a satellite channel with no cooperation and MMSE detector. It is also highlighted the point where $I(\mathbf{x};\mathbf{y}) = r_c \log_2 M$ to let the reader understand the SNR region where they are going to be used. If we instead had to work at low SNR (in relation to the code rate and modulation order), giving information about the weakest bits could have added nothing due to the lower slope of the curve in that region.

Moreover, at high SNRs we could resort to Max-Log-MAP detector, since the approximation in the computation of the LLR will be almost negligible. This means that less computational complexity will be required by user 2.

The adopted quantization scheme is the following: user 2 will compute and then quantize the LLRs associated to each sequence $\mathbf{b}_i$ with b_{L_i} bits, with the constraint set by the side-channel $\sum_i b_{L_i} = b_c$. A value $b_{L_i} = 0$ means that no information about $\mathbf{b}_i$ will be sent. The quantization thresholds are tailored on estimates of the LLRs distributions so that the quantized levels for each $\mathbf{b}_i$ are equally distributed. Regarding the receiver of the user 1, it performs an estimate of the probabilities $p(\hat{y}_{2_k}|x_k)$ similarly to the receiver described in Sec. 2.2.2.

We found that whenever $b_{L_i} \leq 1$ for every position i, a simpler and equivalent approach to design the quantization is clustering based on the MODCOD bit-mapping. We can, in fact, assign a value to $\hat{y}_k^{(2)}$ by grouping symbols that share the same value of the bits we are intending to help. Examples for the 16-APSK with $r_c = 3/4$, 32-APSK with $r_c = 3/4$, and 64-APSK with $r_c = 4/5$ are reported in Fig. 2.7, 2.8, and 2.9, respectively, for $b_c = 2$. We grouped the symbols using the the weakest bits for

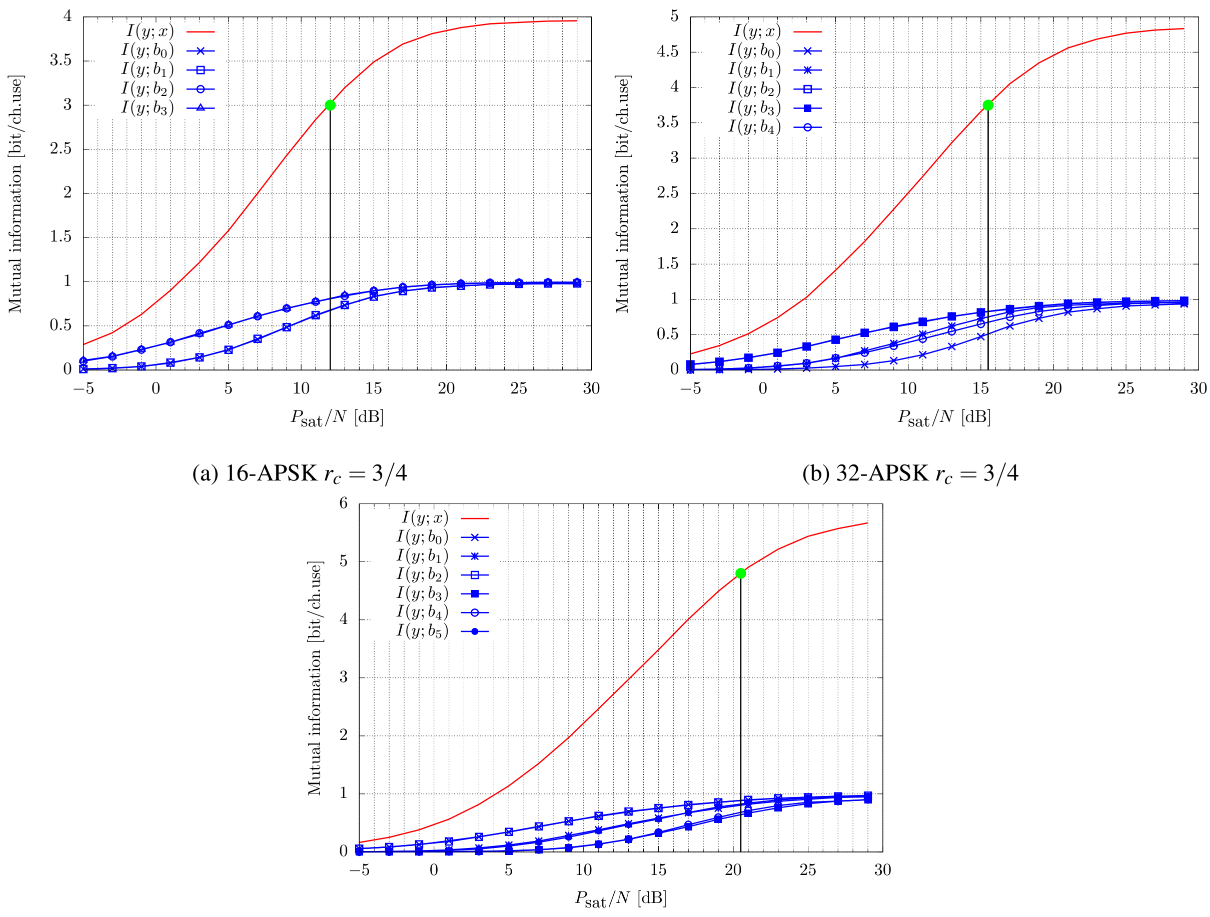

(c) 64-APSK $r_c = 4/5$

Figure 2.6: Mutual Information $I(\mathbf{x};\mathbf{y}^{(1)})$ and $I(\mathbf{b}_i;\mathbf{y})$ of the reference receiver for the analyzed MODCODs. We also highlighted the point where $I(\mathbf{x};\mathbf{y}^{(1)}) = r_c \log_2 M$.

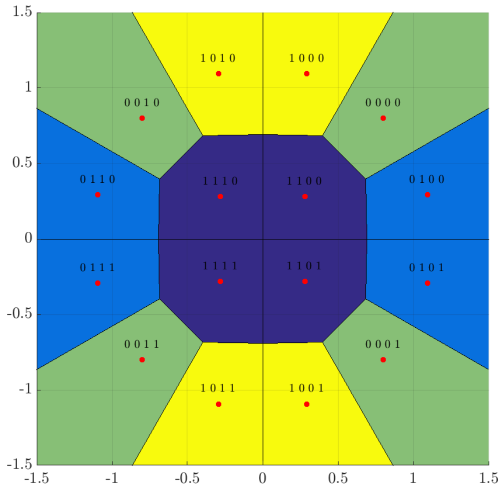

Figure 2.7: Decision regions for 2-bit quantization of the 16-APSK $r_c = 3/4$. Same color means same quantized symbol. This approach is intended to help the first two bits (the weakest ones).

each scheme. It is interesting since this mapping seems effective even though it does not minimize the MSE distance between quantization inputs and outputs.

2.3 Results

We show the possible gains achievable with the schemes mentioned above. The gains in SNR of the C_b function with LLR quantization scheme (LLR in the legend) are reported in Figs. 2.10a, 2.10b, and 2.10c, together with the employed b_{L_i} values. We employed all possible configurations of $[b_{L_0}, \cdots b_{L_{\log_2 M}}]$, where b_{L_i} takes value of 0, 1 or 2 bits, but we show only the configurations maximizing the gain for a given b_c. In Tab. 2.1 we report the bit indices i ordered by the value $I(\mathbf{b}_i;\mathbf{y})$ at the SNR where $I(\mathbf{x};\mathbf{y}) = r_c \log_2 M$. Indices sharing the same $I(\mathbf{b}_i;\mathbf{y})$ value are reported twice and separated by a comma. Looking at Tab. 2.1 we see that Fig. 2.10 tends to follow the foreseen trend of helping the weakest bits. We checked that when it is not, the difference is just on the second decimal digit and could be related to numerical

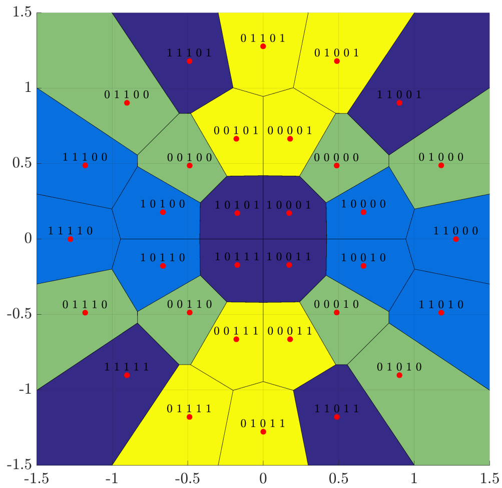

Figure 2.8: Decision regions for 2-bit quantization of the 32-APSK $r_c = 3/4$. Same color means same quantized symbol. This approach is intended to help the first and last bit (the weakest ones).

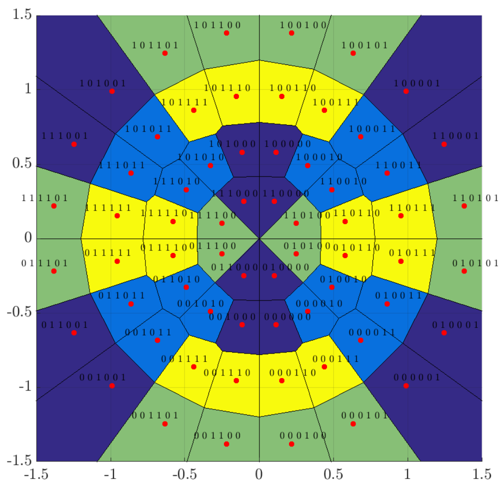

Figure 2.9: Decision regions for 2-bit quantization of the 64-APSK $r_c = 4/5$. Same color means same quantized symbol. This approach is intended to help the fourth and fifth bit (the weakest ones).

approximations. For the sake of comparison, we also reported the gains in SNR for the C_b function with the MMSE receiver and the receiver with modification of BCJR that performs an estimate of the probabilities (PE in the figures). We decided to use C_b as a metric for all of the schemes in order to have a fair comparison. It can be seen that if the number of quantization bits is lower than $\log_2 M$, the LLR scheme seems more convenient.

In Figs. 2.11a, 2.11b and 2.11c we show packet error rate (PER) curves for the three analyzed MODCODs with $b_c = 2$. The gains over the non-cooperative receiver performance match almost exactly those foreseen by the mutual information (the limit set by C_b is also reported in the figure).

Table 2.1: Bit indices i in descending order of $I(\mathbf{b}_i; \mathbf{y})$ for each considered MODCOD.

	1^{st}	2^{nd}	3^{rd}	4^{th}	5^{th}	6^{th}
16-APSK 3/4	4,3	4,3	2,1	2,1	-	-
32-APSK 3/4	4,3	4,3	2	5	1	-
64-APSK 4/5	1,3	1,3	6,2	6,2	5,4	5,4

2.4 Conclusions

In this chapter, we proposed a new scheme for exploiting constrained cooperation in satellite receivers. The constraint is in the capacity of the link between the receivers, where the signal should be quantized. We demonstrated its effectiveness with three different schemes on satellite channels with high order APSK modulation: an MMSE based approach, an approach based on BCJR modifications and a third one based on LLRs quantization. We also saw that the algorithm that works on the quantized version of LLRs has higher gains when the number of quantization bits is lower than the number of bits necessary to represent all the modulation symbols and that there's a simple approach to cluster together symbols and design a quantization scheme when the number of quantization bits is $b_c < \log_2 M$. For channels with higher memory, however, the estimation described in Sec. 2.2.2, has a number of probabilities to es-

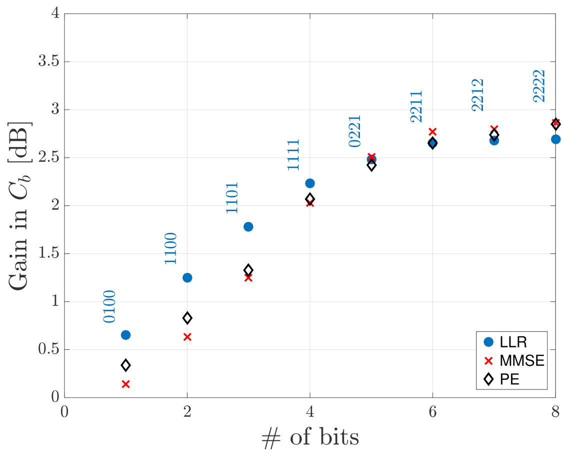

(a) 16-APSK $r_c = 3/4$

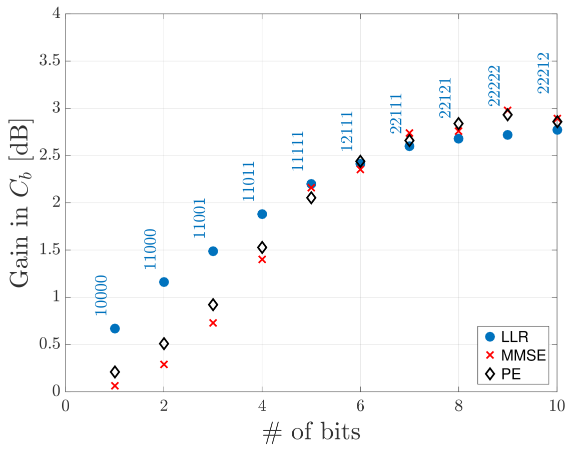

(b) 32-APSK $r_c = 3/4$

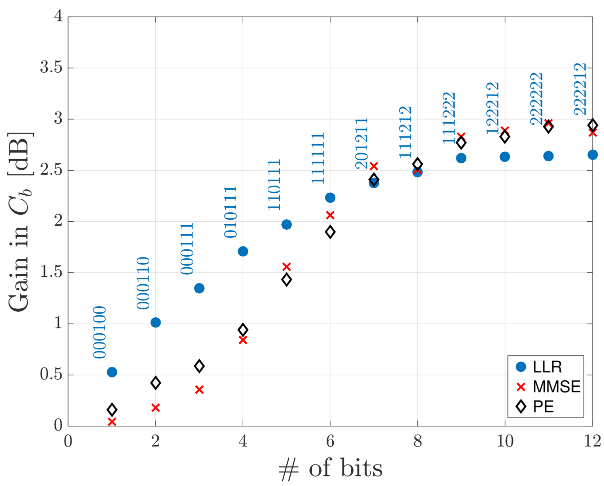

(c) 64-APSK $r_c = 4/5$

Figure 2.10: Gains over the reference scenario in SNR for C_b curves achieved by the different schemes.

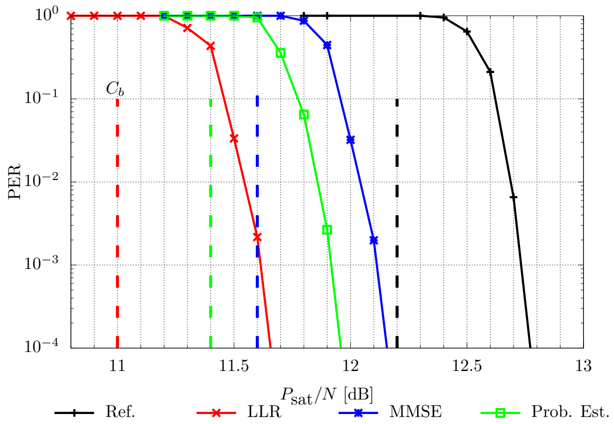

(a) 16-APSK $r_c = 3/4$

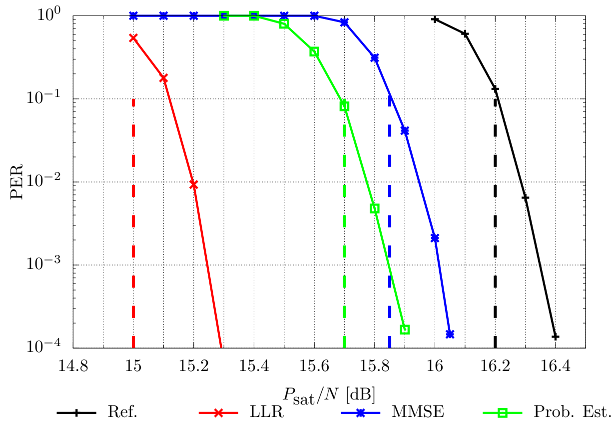

(b) 32-APSK $r_c = 3/4$

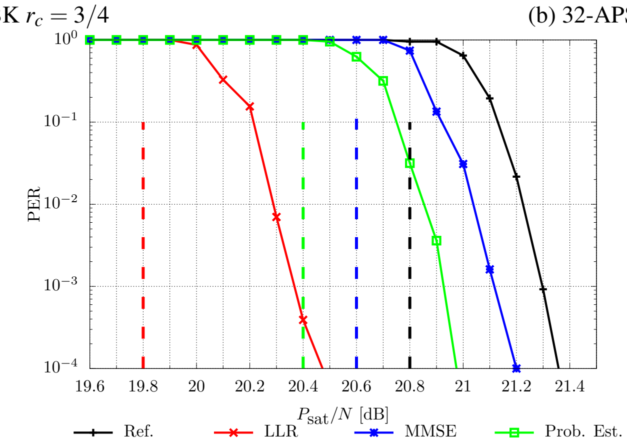

(c) 64-APSK $r_c = 4/5$

Figure 2.11: PER curves for the analyzed MODCODs and $b_c = 2$. The vertical dashed lines mark the achievable information rates in term of C_b. The PER curves of the reference scheme with no cooperation are also reported for comparison purposes.

timate exponential in the memory of the detector. This means that also the training phase for their estimation will be exponentially longer. The LLR-estimation in Sec. 2.2.3, instead, would have the drawback of requiring the helping user to perform a detection with a more complex and slow BCJR with $L \geq 1$. This would introduce more delay in the system and goes against the principle of minimizing the computational demand for the helping user. The MMSE receiver in Sec. 2.2.1, instead, could easily be extended to higher memory channels through the CS framework.

Chapter 3

Advanced Techniques for Earth Observation links

In this chapter, we will apply TFP techniques and more sophisticated receiver architectures to high rate telemetry systems. In this kind of systems, data are generated directly on the satellite and then transmitted to Earth. This allows the use of a signal predistortion algorithm [35, 36, 37], which is expected to better compensate the non-linear effects introduced by the satellite channel with respect to simpler constellation predistortion techniques used in DVB-S2.

This scenario was the object of an activity promoted by the European Space Agency with the aim of introducing possible improvements to the current high rate telemetry standard [38]. We will analyze two different scenarios, with one and two channels, respectively. For both scenarios, we will apply advanced techniques at the transmitter and at the receiver.

3.1 System Model

3.1.1 Single Channel Scenario

The first analyzed scenario, referred to as Scenario 1 in the following sections, is that depicted in Fig. 3.1. The information bits to be transmitted to Earth are mapped on

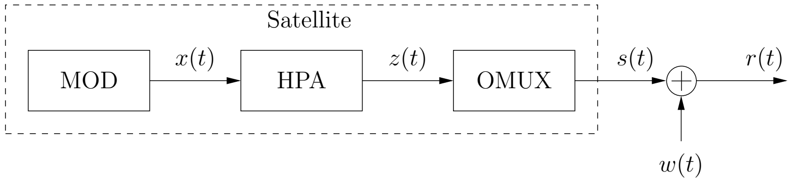

Figure 3.1: Block diagram of the transmitter for Scenario 1.

K symbols of an $M-$ary zero-mean complex constellation to generate the sequence $\{x_k\}_{k=0}^{K-1}$. We can express the complex envelope of the transmitted signal as

$$x(t) = \sum_{k=0}^{K-1} x_k p(t - kT_s)\,, \tag{3.1}$$

where the shaping pulse $p(t)$ is a RRC pulse with roll-off factor β and T_s is the symbol interval. The HPA amplitude modulation/amplitude modulation (AM/AM) and amplitude modulation/phase modulation (AM/PM) characteristics are those foreseen by the DVB-S2 standard [22] and are reported in Fig. 2.4, while the output multiplexer OMUX filter is a 5th order elliptic filter [39] with a ripple of 0.1 dB, passband $W_\mathrm{p} = 600$ MHz and stopband $W_\mathrm{s} = 750$ MHz. The amplitude response of the adopted filter is shown in Fig. 3.2. We consider, as a reference, a system operating with a symbol rate $R_\mathrm{s} = 500$ Mbaud and allowing the use of the static DPD described in [26, 27] and adopted by DVB-S2 systems to help compensating the nonlinear distortions introduced by the HPA. The reference system adopts a shaping pulse with roll-off $\beta = 0.35$, corresponding to a total signal bandwidth equal to 675 MHz. The received signal is then affected by an additive white Gaussian noise process, whose low-pass equivalent $w(t)$ has power spectral density N_0. The received signal has expression

$$r(t) = s(t) + w(t)\,,$$

where $s(t)$ is the signal at the output of the transmitter.

At the receiver, a sufficient statistic is extracted by using oversampling at the output of a front-end filter [25]. A FS MMSE equalizer, then, acts as an adaptive filter, followed by a symbol-by-symbol detector. This detector does not rely on any

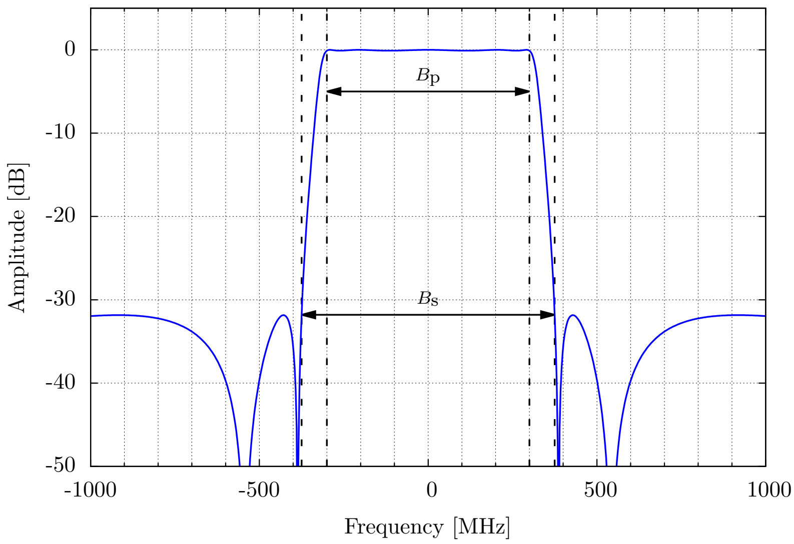

Figure 3.2: Adopted OMUX filter for Scenario 1.

specific signal model and the receiver is adaptive, assuming that sampling frequency and carrier frequency offsets have already been recovered. It has been shown in [24] that this receiver structure represents an excellent trade-off between performance and complexity for a DVB-S2 based system. To evaluate the performance of the proposed architectures we will use, as a figure of merit, the ASE of the system, defined as

$$\mathrm{ASE} = \frac{I_R}{T_s W} \quad [\mathrm{bit/s/Hz}],$$

where I_R is the maximum achievable information rate of the channel. For a system with memory, I_R can be computed by means of the Monte Carlo method described in [5]. If a suboptimal detector is applied, this technique allows to compute an achievable lower bound on the real information rate, corresponding to the information rate of the channel under consideration when that suboptimal detector is adopted, according to the principle of mismatched detection [7] (see Chapter 1).

The ASE will be computed as a function of P_{sat}/N, where P_{sat} is the saturation power of the HPA, and $N = N_0 W$ is the noise power in the considered bandwidth.

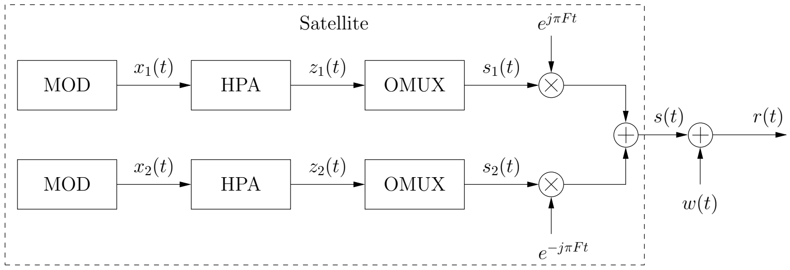

Figure 3.3: Block diagram of the transmitter for Scenario 2.

3.1.2 Two Channels Scenario

The second analyzed scenario (Scenario 2) is a direct extension of the previous one when two transmitters on the same satellite are available. The block diagram of the transmitter, in this case, is shown in Fig. 3.3. The two HPAs and OMUX filters are identical, and they have the same characteristics as those of the previous section. The reference architecture still has the same transmission parameters, namely symbol rate $R_s = 500$ Mbaud and RRC pulses with roll-off $\beta = 0.35$. Moreover, for the reference scenario, we will consider the two channels to be spaced in frequency by $F = 750$ MHz. This value ensures that the passbands of the two OMUX filters do not overlap with each other, leaving an appropriate guard band between the two channels. The receiver will adopt two FS-MMSE equalizers followed by two Single User Detector (SUD), as already done in the single channel reference scenario.

To compute the ASE of this system, a bandwidth definition is required. In order to define the overall signal bandwidth, we can proceed as follows.

1. Compute the information rate I_R of the system as the sum of the information rates of the two channels.

2. After the signals are shifted in frequency, insert a filter with the same shape as the OMUX filters, but with passband W_f large enough to leave the two signals, and hence I_R, unchanged.

3. Progressively reduce W_f until a reduction in I_R is observed.

4. Define the bandwidth of the system as the smallest value of W_f which causes a reduction of I_R not greater than 1% with respect to the case without the filter.

With this procedure, we defined the reference bandwidth as $W_\mathrm{f} = 1320$ MHz, and we can compute the ASE as

$$\mathrm{ASE} = \frac{I_R}{T_\mathrm{s} W_\mathrm{f}} \quad [\mathrm{bit/s/Hz}].$$

Again, the ASE will be computed as a function of P_sat/N. However, in this case P_sat is the overall available power of the HPA, and hence it is twice as much as the power available in Scenario 1. Also in this case, $N = N_0 W_\mathrm{f}$ is the noise power in the considered bandwidth.

3.2 Optimization of the Reference Architecture

For the optimization of this reference system, we consider the application of advanced techniques at both the transmitter and receiver sides. The analyzed solutions can be summarized as follows.

The optimization of the symbol rate and of the signal bandwidth. The symbol rate and the roll-off factor of pulse $p(t)$ can be jointly optimized to find the best setting for a fixed bandwidth of the OMUX filter. Hence, we will consider the adoption of lower roll-off values and an increased symbol rate. This kind of optimization is similar to that performed in [23] for the extensions of the DVB-S2 system (DVB-S2X [1]).

The application of faster-than-Nyquist or time-frequency packing. In satellite systems, orthogonal signaling is often adopted to avoid ISI at least in the absence of non-linear distortions. When finite-order constellations are considered, it is well known that the ASE can be improved by relaxing the orthogonality condition, thus intentionally introducing a certain amount of controlled ISI. In this case, the systems are working in the domain of the *Faster-than-Nyquist* paradigm [40, 41, 42, 43] or its extension known as *time packing* [44, 20, 45]. The effect of this technique is somehow similar to the increase of the signal bandwidth, as shown in [45]. In fact, for fixed transmitter filter bandwidths, an increase of the signal bandwidth will result in an increase of ISI. However, the use of time packing adds another degree of freedom that can be properly exploited. From an operational point of view, we can define the symbol interval as $T_s = \tau T$, where T is half of the main lobe duration of $p(t)$ and $\tau \leq 1$ is the time-packing factor, which will be properly selected to maximize the efficiency of the system. The same concept has been extended to the frequency domain, when more channels are present. Hence, in Scenario 2, we can also apply the *frequency packing* technique, by reducing the frequency spacing F and jointly increasing the symbol rate, thus introducing controlled ICI.

The use of a more sophisticated receiver. The increased ISI (in both scenarios) and ICI (in Scenario 2) introduced by the two previously mentioned techniques can be more effectively coped with by adopting more sophisticated receiver architectures. In particular, we will adopt the adaptive CS receiver proposed in [15], which consists of an FS equalizer, an adaptive CS filter and a BCJR detector [6]. This receiver structure is based on the CS technique [12], which allows to design the information-theoretically optimal mismatched receiver for a given reduced complexity. When the channel memory at the detector is set to $L = 0$, this scheme is equivalent to the FS-MMSE receiver of the reference scenario. Moreover, for Scenario 2, the adaptive CS filters can be followed not only by a SUD, as in Scenario 1, but also by a Multiuser Detector (MUD), which is expected to better handle the ICI arising from the application of the frequency packing technique, at the price of an increased complexity of the detection stage [46]. For the SUD receiver of Scenario 2, we also implemented a receiver based on the IC-CS [13] and showed the attainable gains. Moreover, to fully exploit the available bandwidth, we propose an alternative transmitter structure, which consists in removing the two OMUX filters at the output of the transmitters, and introducing a single large filter with bandwidth W_{f}. In this bandwidth, we will allow the two signals to be as overlapped as possible, and we will adopt both the SUD and the MUD. The block diagram of the transmitter for this new architecture is shown in Fig. 3.4, where the BPF is a band-pass filter with bandwidth W_{f}. It should be noted, however, that the combination of two Radio Frequency (RF) signals overlapping in frequency can cause significant power losses. This issue will be briefly addressed later.

The use of the Alamouti space-time block code. For Scenario 2, we will also con-

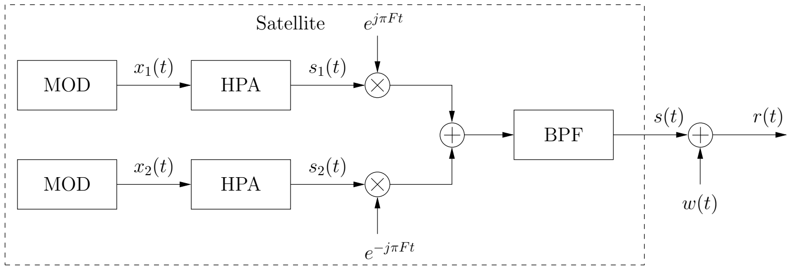

Figure 3.4: Evolution of the transmitter for the Scenario 2.

sider the application of the Alamouti space-time block code [47] as a convenient alternative. Unlike what happens in [47], we do not use the Alamouti scheme to achieve a diversity gain, but as a way of orthogonalizing the two signals. In this scheme, the two transmitters exchange the two information sequences in two successive transmission intervals. At the receiver, two consecutive observed sequences are properly processed and then fed to two SUDs. In this way we can always transmit fully overlapped signals and perform only lower complexity operations at the receiver. To preserve the orthogonality of the two signals, in this approach, the same information has to be transmitted twice over two consecutive intervals. Moreover, the nonlinear effects introduced by the HPA prevent an ideal cancellation of the interfering signal, thus affecting the performance of the detector. More insights on the application of the Alamouti technique on a nonlinear satellite channel can be found in [48], where it is also demonstrated that the Alamouti scheme is convenient when compared to Time Division Multiplexing (TDM) or Frequency Division Multiplexing (FDM) schemes. On an ideal channel, the three schemes are perfectly equivalent; however, TDM requires that, in each transmission slot, each transmitter uses double power, which might not be a feasible solution in a peak-power limited channel such as that under consideration. The performance of FDM, on the other hand, is significantly degraded by the interference of the adjacent channel, which derives from the spectral regrowth caused by the HPA [48].

The use of a more advanced predistortion algorithm. As mentioned, for the reference scenario, we will adopt the static DPD of [26, 27]. This algorithm consists

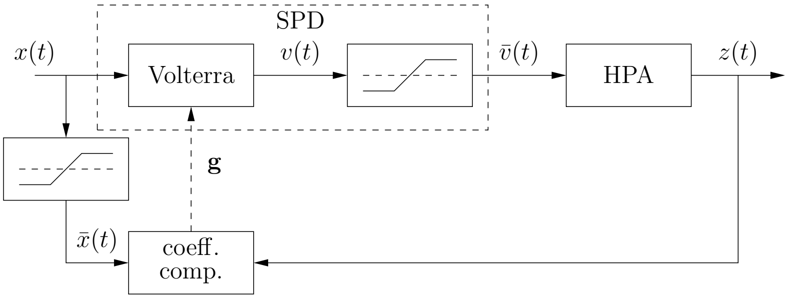

Figure 3.5: Block diagram of the proposed SPD.

of a training phase, in which the predistorted constellation is computed based on the channel outputs. The information bits are then mapped on this constellation instead of using the real one. This approach is convenient in a scenario like the DVB-S2 model, where predistortion takes place at a transmitter on the ground, that is, remotely from the source of nonlinearity, and not directly before the HPA. In this scenario, instead, data are generated directly on the satellite, and they can be predistorted exactly before the amplifier. This fact allows us to use a Signal PreDistorter (SPD) instead of a DPD. SPDs have been widely studied in the literature [35, 36, 37] due to their ability to work on the samples of the continuous time signal rather than on the transmitted symbols.

We will now introduce a new signal predistortion algorithm, whose performance will be investigated in the next section. The block diagram of the proposed SPD is shown in Fig. 3.5, and it is composed of two main blocks. The block labeled as “Volterra” takes as input the signal (3.1) and outputs the signal

$$v(t) = \sum_{s=0}^{S} g_s x(t) |x(t)|^{2s}, \tag{3.2}$$

that is, a memoryless Volterra series of order $2S+1$ taking into account odd order terms only. The second block is a hard limiter, which clips the amplitude of the signal and whose input-output relationship can be expressed as

$$\bar{v}(t) = \begin{cases} v(t) & \text{if} \quad |v(t)| \leq 1 \\ 1 & \text{otherwise.} \end{cases}$$

We have verified that the presence of this hard limiter significantly improves the performance, as in this way the nonlinear part of the characteristic is completely avoided. The complex coefficients $\mathbf{g} = \{g_s\}_{s=0}^{S}$ in (3.2) are selected to minimize the mean-square error between the transmitted hard-limited signal $\bar{x}(t)$ and the signal at the output of the HPA, $z(t)$:

$$\mathbf{g} = \underset{\mathbb{C}^{S+1}}{\operatorname{argmin}} \mathrm{E}\left[|z(t) - \bar{x}(t)|^2\right] . \tag{3.3}$$

During the training stage, the block "coefficients computation" in Fig. 3.5 performs the minimization (3.3) through the algorithm described in [49] and included in the nonlinear optimization package [50]. We point out that this predistortion scheme can also be used jointly with the described DPD (we will denote this as DSPD scheme): the predistortion of the constellation can be used to further contrast the residual distortions that the SPD alone has not been able to invert.

3.3 Numerical Results

In this section, we show the results, in terms of ASE, of the proposed transceiver techniques, for the two scenarios under consideration. We adopt the $M-$ary Phase Shift Keying (PSK) and APSK constellations foreseen by the CCSDS standard [38], with cardinality ranging from 4 (QPSK) to 32. For 64APSK, we adopt a constellation introduced by the DVB-S2X standard [1], which ensures slightly better performance with respect to that of CCSDS. Unless otherwise stated, the ASE curves will be computed as the envelope of the ASEs of all modulation formats. This means that, for each value of P_{sat}/N, we will choose the modulation format achieving the best ASE. Moreover, for each case, the IBO of the HPA will be optimized to maximize the ASE.

3.3.1 Scenario 1

Fig. 3.6 shows the ASE of the system with an optimized symbol rate, in comparison with the reference scenario. The roll-off factor is set to $\beta = 0.35$ for all curves. We also compare the performance of the static DPD with the SPD and DSPD schemes proposed in the previous section, with $S = 3$ (that is, the signal is modeled as a 7th order nonlinearity), for increasing values of the memory considered at the receiver, $L = 0$, 1. The details on the symbol rate for the curves of Fig. 3.6 are reported in Table 3.1 for DPD and SPD. The first thing we notice is that the SPD is clearly convenient over the DPD, with the DSPD that grants some further limited gains in some parts of the curves. We also notice that, in the medium-low P_{sat}/N range, increasing the complexity of the detector can provide only very limited advantages. More relevant differences arise in the high P_{sat}/N region, where the increased memory can better cope with the interference introduced by the high symbol rate values. In all cases, however, the gains over the reference scenario are significant. We also mention that we have performed the same analysis by using reduced roll-off values, namely 0.2 and 0.1, but the results do not improve with respect to the reference value of 0.35. This is reasonable because, by optimizing the symbol rate, we are also selecting the best signal bandwidth, and hence a further optimization of the roll-off is not required. Interestingly, the proposed SPD allows the system to work with a much lower IBO with respect to the DPD. In fact, while the SPD requires an IBO of 3 dB only for 64APSK, the DPD needs an IBO of 3 dB for 16APSK, 6 dB for 32APSK, and 9 dB for 64APSK, to achieve the presented performance. A higher IBO also has a negative impact on the HPA efficiency, and, in turn, on the power dissipated on board.

We next consider the application of time packing. For this analysis, only the DPD has been applied, but similar results can be obtained for the SPD. Fig. 3.7 shows the ASE for QPSK and 8PSK when the value of τ has been optimized. The memory of the BCJR has been set to $L = 4$, which, we found, is practically optimal for this scenario. Both curves have been computed starting from the reference symbol rate $R_{\mathrm{s}} = 500$ Mbaud. We see that, although the symbol time is optimized, time packing cannot reach the same performance as transmission with orthogonal signaling with increased symbol rate. In fact, Fig. 3.7 also reports the ASE of 8PSK and 16APSK

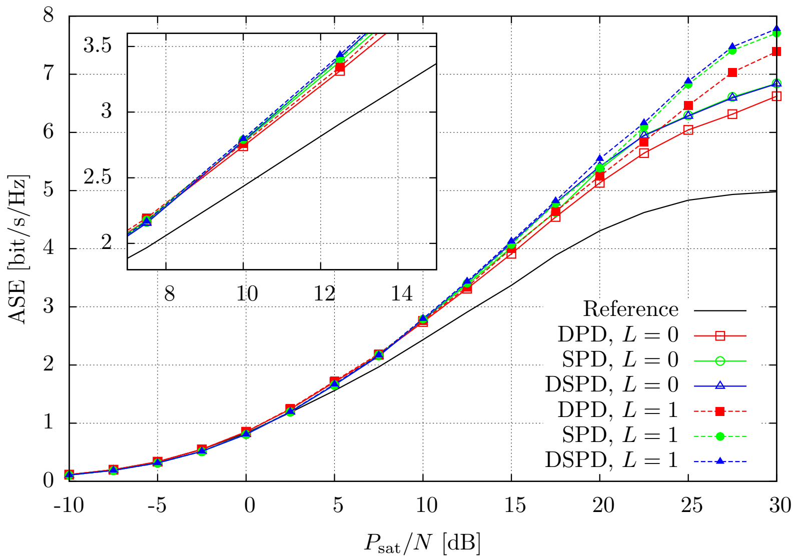

Figure 3.6: ASE for Scenario 1 and optimized symbol rate.

Table 3.1: Optimized symbol rate R_s (in Mbaud) for the curves in Fig. 3.6.

P_{sat}/N [dB]	DPD				SPD			
	$L=0$		$L=1$		$L=0$		$L=1$	
	M	R_s	M	R_s	M	R_s	M	R_s
-10	8	500	8	500	4	550	4	550
-5	8	550	8	550	8	500	8	500
0	8	600	8	600	8	550	8	550
5	8	650	8	650	8	650	8	650
10	16	650	16	650	16	650	16	650
15	32	650	16	850	32	650	16	800
20	64	650	32	800	64	650	64	650
25	64	650	64	800	64	650	64	800
30	64	700	64	800	64	700	64	800

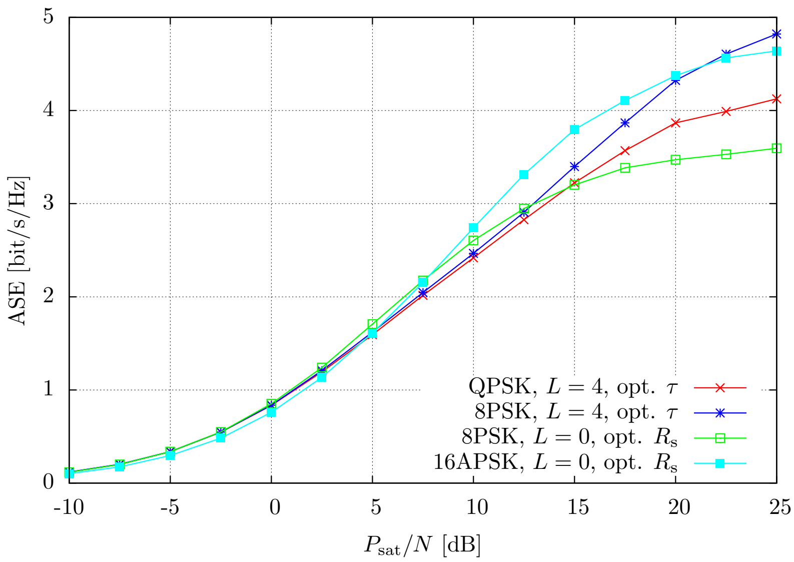

Figure 3.7: ASE for Scenario 1 and time packing.

with optimized symbol rates. The latter curves achieve higher values of ASE with a much lower complexity, relying only on a symbol-by-symbol detector, with $L = 0$. This result is somewhat expected, as it is in line with that obtained for a DVB-S2X scenario in [24], which shows that the potential of time packing on the satellite channel is very limited. However, it is important to remember that a sort of alternative to time packing is already achieved by increasing the symbol rate of the signal. In fact, both techniques introduce interference to the signal.

Then, we investigate more in detail the performance of the proposed SPD. Fig. 3.8 reports the ASE for orders of the SPD increasing from 1 to 7, when the detector with memory $L = 0$ is adopted (similar conclusions can be drawn when $L = 1$). We see that a 3rd order Volterra series is already practically optimal. We also notice that the DSPD has significant advantages when the 1st order series is adopted, while the gains are much more limited in the other cases. This analysis proves that most of the nonlinear effects are inverted by the SPD. Finally, Fig. 3.9 shows the PSD for the predistorted signal at the output of the OMUX filter. We see that the proposed

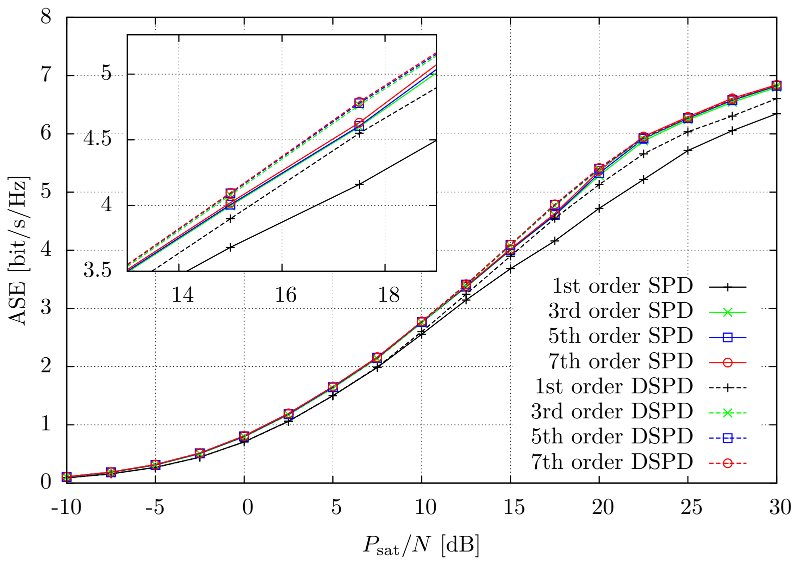

Figure 3.8: SPD and DSPD performance in Scenario 1.

SPD does not increase the side lobes of the spectrum with respect to the absence of predistortion (*no pred.* PSD). The transmission parameters for Fig. 3.9 are the optimal ones at $P_{\text{sat}}/N = 10$ dB, but the same happens for other configurations and for the DSPD scheme.

3.3.2 Scenario 2

Following from the results obtained for Scenario 1, in Scenario 2 we will not consider the application of time packing as a possible solution, and we will fix the roll-off factor of the shaping pulse to 0.35. Moreover, for the sake of clarity, we will not present results for the SPD. We have, however, verified that the performance of the SPD is practically equivalent to that of the DSPD scheme.

Fig. 3.10 compares the envelope of the ASE for different transceiver schemes, all considering a memory $L = 0$ at the detector. In particular, the curve labeled *with OMUX* only differs from the reference in the symbol rate and central frequency of the two channels, which have been selected to maximize the ASE. As we see, this

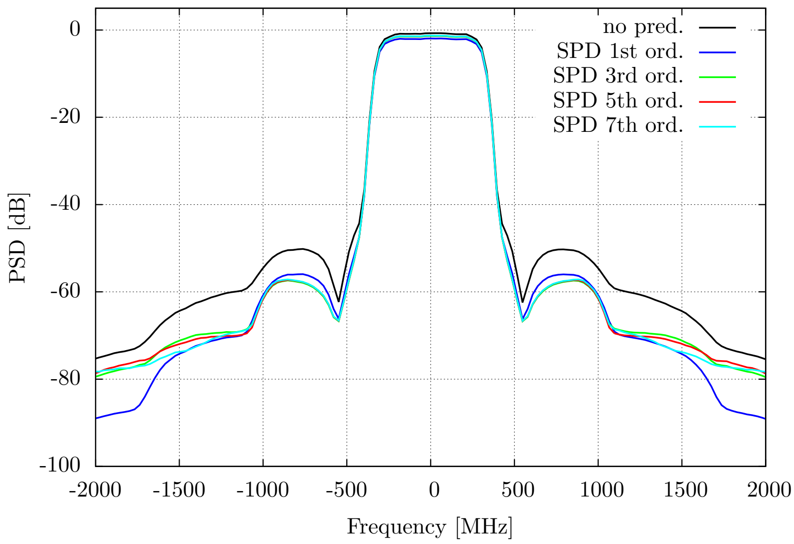

Figure 3.9: PSD of the transmitted signal with SPD in Scenario 1, 16APSK, IBO = 0 dB, $R_s = 650$ Mbaud.

optimization alone allows significant gains. Further gains can be achieved by removing the two OMUX filters and introducing the single filter with bandwidth W_f (*no OMUX* curves). In this case, we can use the MUD to fully exploit the ICI generated by the frequency packing, achieving excellent performance at the price of an increased complexity with respect to the SUD. Finally, the Alamouti scheme can outperform the SUD with basically the same complexity, although it is still far from the MUD. To conclude the analysis, we can confirm the superiority of the proposed (D)SPD scheme over the DPD for all receiver architectures.

Next, we increase the memory considered at the detector. We point out that this investigation has been carried out only for the schemes without the two inner OMUX filters. This is because a higher complexity detector is needed to cope with the increased interference which arises when the filters are removed. The resulting ASE curves are shown in Fig. 3.11. If we compare them with the corresponding curves in Fig. 3.10, we see that both the SUD and the Alamouti schemes have only small benefits with respect to symbol-by-symbol detection, and only in the high P_{sat}/N range.

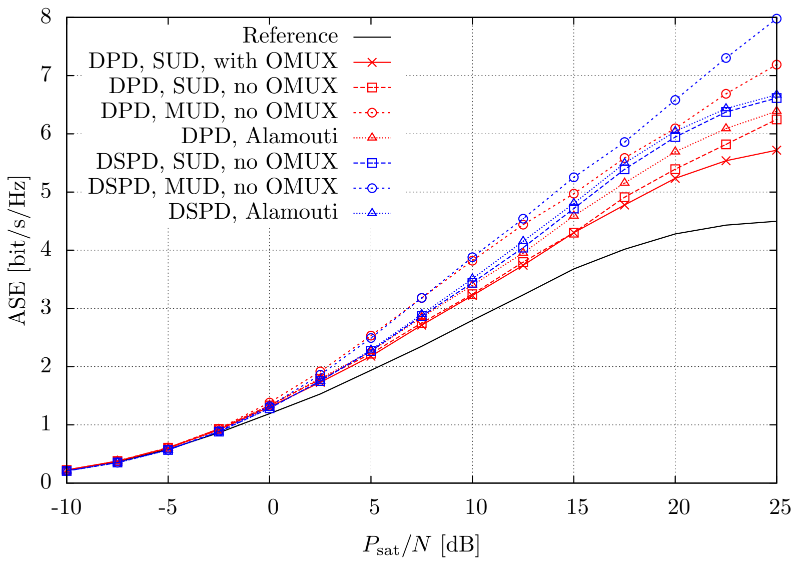

Figure 3.10: ASE for Scenario 2 with $L = 0$.

For complexity reasons, we have not simulated the performance of the MUD with $L = 1$. However, we see that the symbol-by-symbol MUD in Fig. 3.10 has better performance than the other two receiver schemes, even when part of the memory is taken into account at the detector.

Let us now better characterize the behavior of the MUD in this scenario. Table 3.2 reports the optimized values of symbol rate R_s and frequency spacing F for the scheme adopting the DSPD and the MUD with $L = 0$. We can notice that, as P_{sat}/N increases, the symbol rate increases and the frequency spacing quickly falls to 0, allowing the two signals to be completely overlapped in frequency. The same behavior can be observed with the DPD instead of the DSPD. Fig. 3.12 shows how the ASE varies as a function of R_s for increasing values of P_{sat}/N, for the MUD receiver. While the global maximum is that reported also in Table 3.2, it is interesting to notice that another lower peak arises in correspondence with a lower symbol rate. If we compare this second peak with the curves in Fig. 3.10, we see that it exactly corresponds to the ASE achieved by the SUD receiver. Moreover, we have verified that

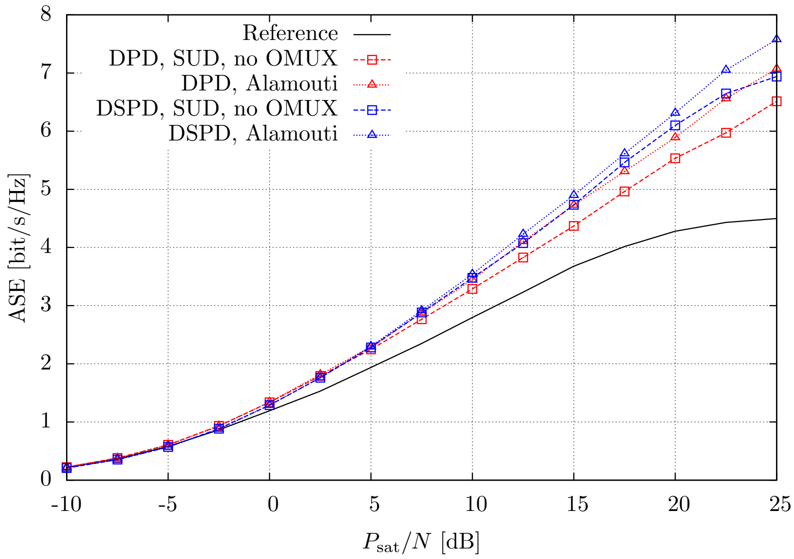

Figure 3.11: ASE for Scenario 2 with $L = 1$.

Table 3.2: Details of the ASE in Fig. 3.10 for the DSPD and the MUD receiver.

P_{sat}/N [dB]	M	R_s [Mbaud]	F [MHz]
-10	4	572	594
-5	8	660	594
0	8	1364	66
5	8	1408	0
10	8	1408	0
15	16	1452	0
20	32	1452	0
25	64	1452	0

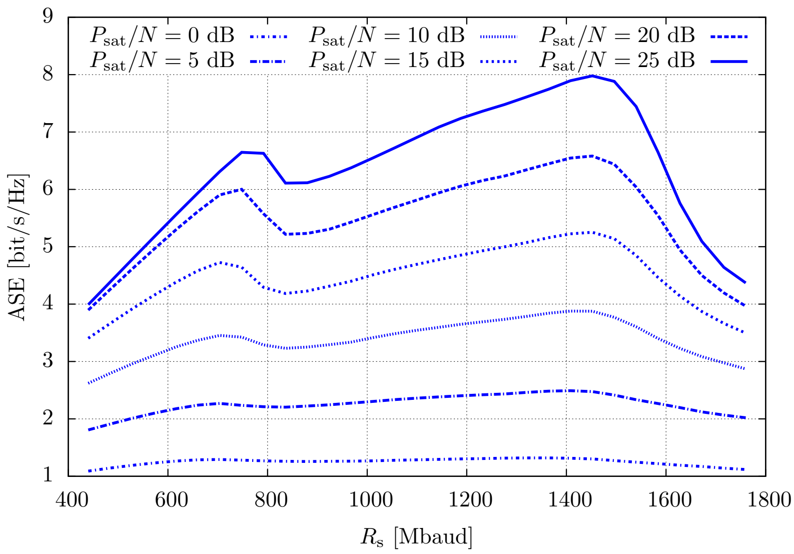

Figure 3.12: ASE as a function of R_s for the MUD receiver.

also the values of R_s and F associated with the second peak are almost the same as the optimized values for the SUD. We can conclude that the second peak corresponds to a combination of symbol rate and frequency spacing in which the impact of ICI is almost negligible, and hence the SUD and the MUD have the same performance. This fact can be verified in Fig. 3.13, which reports the ASE and the optimal frequency spacing F for each value of R_s, for $P_{sat}/N = 25$ dB. The value of F corresponding to the second peak is large enough to practically avoid any overlap of the two signals. The same behavior is observed for other values of P_{sat}/N.

It has been proved in [48] that, in a peak-power limited scenario with multiple transmitters and a MUD at the receiver, it is convenient to adopt PSK constellations rather than APSKs. Moreover, it has been shown in [51] that a phase shift of π/M between the two constellations ensures a simple design and good performance. Fig. 3.14 reports the ASE as a function of R_s with these phase-shifted PSK constellations. The peak of the ASE is almost the same as that achieved in Fig. 3.12 with APSKs. However, the second peak is much lower, to indicate that this configuration is not suitable

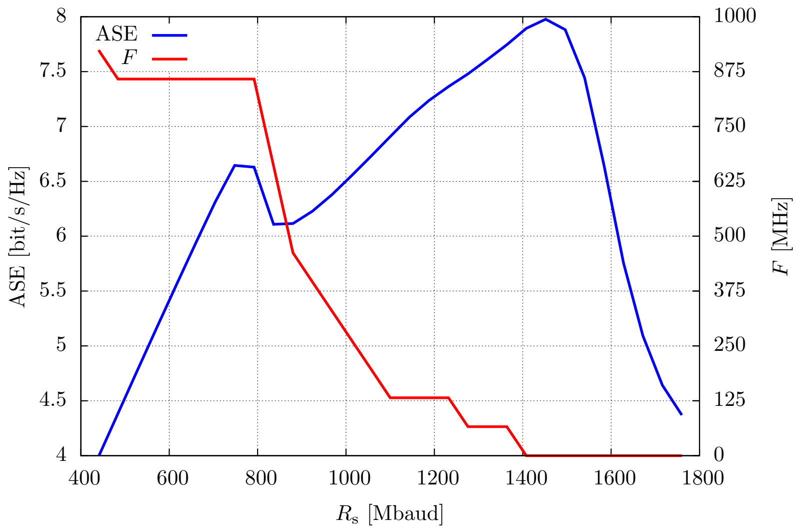

Figure 3.13: ASE and F as a function of R_s for the MUD receiver and $P_{sat}/N = 25$ dB.

for single-user detection.

It is interesting to see also the improvement that can be achieved through the use of the CS receiver extension proposed in [13] and [14]. As explained in Chapter 1, it allows an interference cancellation based on soft-symbol feedback. After a first iteration between the detector and the decoder, the soft-symbols are computed, the filters and the trellis are updated according to the quality of the soft-symbol feedback, and then the soft-symbols are filtered and removed from the received signal samples. This procedure is thus iterated since at each iteration between detector and decoder the quality of the feedbacks should improve. The problem is that it is not possible to compute the AIR of this receiver. In fact, the receiver is changing at each iteration. The only way to test its performance is by using practical codes, testing its PER. To have a fair comparison, we computed also the PER using a simple CS detector that performs an iterative detection and decoding, without interference cancellation (i.e., the filter and trellis remain the same at each iteration). We employed in both the cases the DVB-S2X LDPC codes, with a maximum of 50 iteration at the decoder

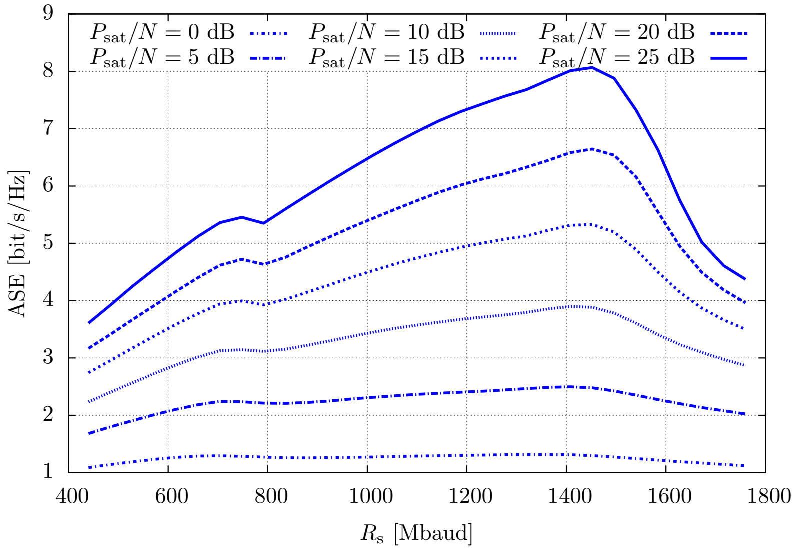

Figure 3.14: ASE as a function of R_s for the MUD receiver and PSK constellations.

and 5 iterations between detector and decoder. We show for reference also the P_{sat}/N value at which the receiver should reach the coding-modulator efficiency $r_c \log_2 M$ with the non-iterative CS. Fig. 3.15 and Fig. 3.15 show the attainable results with an 8-PSK and a 16-APSK, employing $R_s = 800$ MHz. The fact that IC-CS receiver with $L = 0$ outperforms the information rate limit is not surprising, since that is a valid upper bound only for the CS without IC. With an 8-PSK, the detector with $L = 0$ and IC has almost the same performance of a detector with $L = 1$ and no IC, while for the 16-APSK the loss is wider. However, the gap between the detector with and without IC for $L = 0$ is remarkable (~ 3 dB and ~ 10 dB for the 8-PSK and 16-APSK, respectively). It has to be noticed that for $L = 0$ the IC-CS becomes an MMSE receiver with interference cancellation [52, 53, 54]. However, a memory $L \geq 0$ is not useful in this case for an IC receiver: the channel memory introduced by the bandwidth optimization is almost completely captured by a detector with $L = 1$ without performing IC. So, there would be no interference to be cancelled with $L = 1$ for an IC-CS detector, and the receiver would become only more complex, without

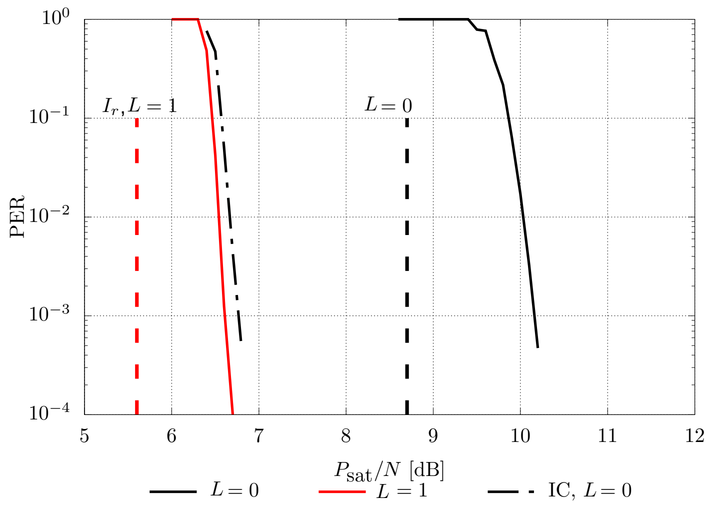

Figure 3.15: PER performance comparison between the simple CS and IC-CS detector, using an $8-$PSK with $r_c = 23/36$ at $R_s = 800MHz$.

any gain in SNR.

We also want to add a comment on some of the theoretical results in this section. For Scenario 2, our results assumed that an ideal combination of the two signals in RF after the HPA is possible. However, the combining of RF of two signals overlapping in frequency will incur a significant loss in the order of 3 dB. Hence, to take into account this effect, the optimized curves of Figs. 3.10 and 3.11 have to be shifted by 3 dB to the right. We can clearly see how in this case the possible gains over the reference architecture are much more limited. A more effective way to exploit the two available HPAs is to combine them to form an equivalent HPA with double power. This solution reduces to a single-carrier scenario with double power, and hence it is a direct extension of Scenario 1. The corresponding ASE can be simply achieved by shifting the curves in Fig. 3.6 by 3 dB to the left.

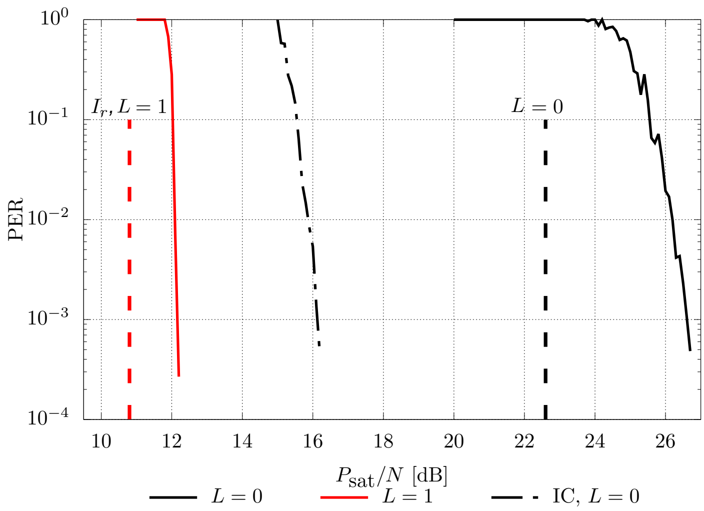

Figure 3.16: PER performance comparison between the simple CS and IC-CS detector, using an 16−APSK with $r_c = 3/4$ at $R_s = 800MHz$.

3.4 Conclusions

We have analyzed two different high rate telemetry scenarios, with one and two channels, respectively. We have shown that, in both cases, significant spectral efficiency gains are possible with respect to the current configuration through the application of advanced techniques at the transmitter and at the receiver. In particular, we have proposed a new signal predistortion algorithm, which exhibits very good performance in the considered scenarios. We have also shown how the proposed signal predistorter can be combined with classical data predistortion techniques, to further enhance the performance. We have then optimized the symbol rate and introduced more sophisticated detection algorithms. For the single-carrier scenario, the proposed solutions allow gains of about 3 dB over the reference architecture at a spectral efficiency of 4 bit/s/Hz. For the scenario with two channels, we have also demonstrated that the application of frequency packing, coupled with the proposed signal predistorter at the transmitter and a multiuser detector at the receiver, can achieve excellent results when compared with all other techniques, at the price of an increased complexity of the detection stage. We have also proposed the use of the Alamouti space-time block code as a lower complexity alternative. For this scenario, the gains with respect to the reference architecture vary from 4 to 7 dB at a spectral efficiency of 4 bit/s/Hz, depending on the adopted transceiver scheme. Furthermore, we showed that on the two channels scenario with an optimized symbol-rate value, the IC-CS at $L = 0$ has a significant gain compared to a CS receiver with the same memory (~ 3 dB for 8-PSK and ~ 10 dB for 16-APSK). For an 8-PSK constellation, the IC-CS at $L = 0$ reaches almost the same performance of a CS receiver with $L = 1$ while the 16-APSK shows a larger loss of ~ 4 dB.

Chapter 4

LEO Satellite Receiver for LoRa Modulated Signals

The IoT devices are becoming widespread and used for many different purposes. They make use of different transmission schemes and protocols and need gateways to connect to the Internet. However, it is hard to have a complete coverage for the communication from the IoT device to the gateway (uplink), especially in rural areas. A swarm of LEO satellites could thus help in these scenarios, by relaying the messages intended for the gateway when the devices are located in areas far from the cities. We base the study on one of the most promising Low Power-Wide Area Network (LPWAN) solution: LoRa. These devices work with a proprietary modulation format at physical layer [2]. Higher layers are defined in the LoRaWAN specifications by the LoRa Alliance [55].

In this chapter, we analyze the LoRa modulation and its receiver scheme. Then, we propose an improved receiver to cope with typical LEO satellite communications impairments (i.e., Doppler shift and Doppler rate).

This is the foundation for the realization of a complete system simulator that includes the interference coming from all the users in the field of view of the satellite. The description of this simulator and the results of the study can be found in [3].

4.1 Lora signal and its properties

The complex envelope of a LoRa signal can be expressed as

$$s(t)=\sqrt{\frac{2E_{\mathrm{s}}}{T}}\exp\left\{j2\pi B\int_{-\infty}^{t}\left[\sum_{k}\Gamma(\tau-kT;a_k)\right]d\tau\right\} \tag{4.1}$$

where E_{s} is the energy per information symbol, T the symbol interval, B a proper parameter ($B=125$, 250, or 500 kHz in the LoRaWAN standard), $\{a_k\}$ the transmitted symbols belonging to the alphabet $\{0,1,\ldots,N-1\}$, being the cardinality N a power of 2 and,

$$\Gamma(\tau;a_k)=\mathrm{mod}\left(\frac{\tau-a_kT/N}{T}\right)\mathrm{rect}\left(\frac{t}{T}\right). \tag{4.2}$$

In (4.2), the $\mathrm{mod}(\cdot)$ function is the modulo operation in $[-0.5,0.5)$. We will define $\mathrm{SF}=\log_2 N$ ($7\leq \mathrm{SF}\leq 12$ in the LoRaWAN standard). Parameters B, N, and T are related through the equation

$$BT=N=2^{\mathrm{SF}}. \tag{4.3}$$

This means that, for a given bandwidth B, the higher the alphabet's cardinality N, the higher the symbol duration T. Fig. 4.1 reports all possible functions $\Gamma(t;a_k)$ for different values of a_k in the case of $\mathrm{SF}=2$ ($N=4$). This parameter choice is not foreseen by the standard but is useful to easily understand the modulation format.

This modulation format is characterized by the following important properties:

1. it has a constant envelope (and thus it is insensitive to nonlinear distortions);

2. it has a continuous phase (and thus its spectrum is compact);

3. it has no memory;

4. the occupied bandwidth is B (with good approximation).

Properties 1 and 2 are obvious from the complex envelope expression (4.1). Property 3 easily follows from the definition of $\Gamma(t;a_k)$ in (4.2). In fact, the integral of $\Gamma(t;a_k)$ is zero, no matter the value of a_k. Thus, if we consider the interval $[kT-T/2,kT+$

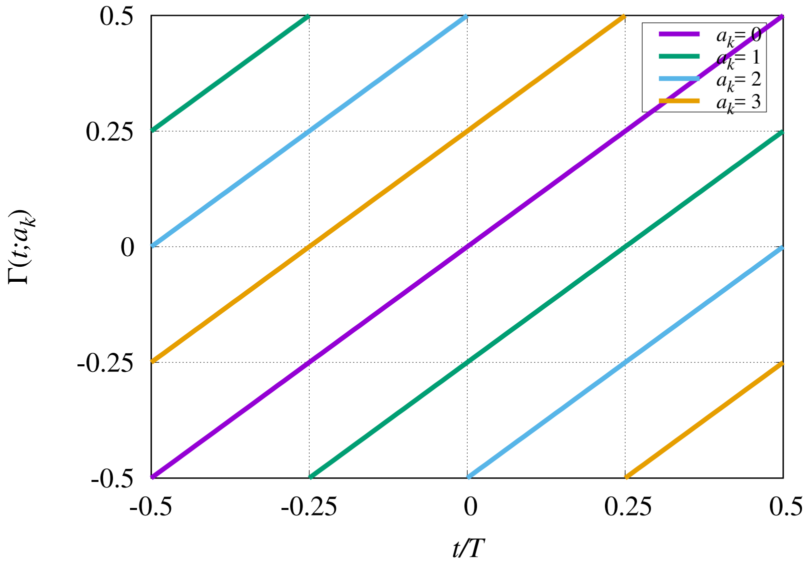

Figure 4.1: Function $\Gamma(t;a_k)$ for different values of a_k in the case $\mathrm{SF}=2$.

$T/2]$, the phase of the complex envelope will be the same (θ_0) at the beginning and at the end of the interval. This modulation is thus memoryless. The shape of the function

$$\Lambda(t;a_k) = \int_{-T/2}^{t} \Gamma(\tau;a_k)\,d\tau$$

is shown in Fig. 4.2 for $\mathrm{SF}=2$.

We will now demonstrate property 4 by computing the PSD of the LoRa signal. Being the modulation memoryless, we may express its complex envelope as

$$s(t) = \sum_k \xi(t-kT;a_k) \tag{4.4}$$

where $\xi(t-kT;a_k)$ is the slice of signal, with support in $[kT-T/2, kT+T/2]$, corresponding to symbol a_k and has expression

$$\xi(t-kT;a_k) = \sqrt{\frac{2E_\mathrm{s}}{T}}\exp\left\{j2\pi B\int_{kT-T/2}^{\min(t,kT+T/2)}\Gamma(\tau-kT;a_k)\,d\tau\right\}\mathrm{rect}\left(\frac{t}{T}\right).$$

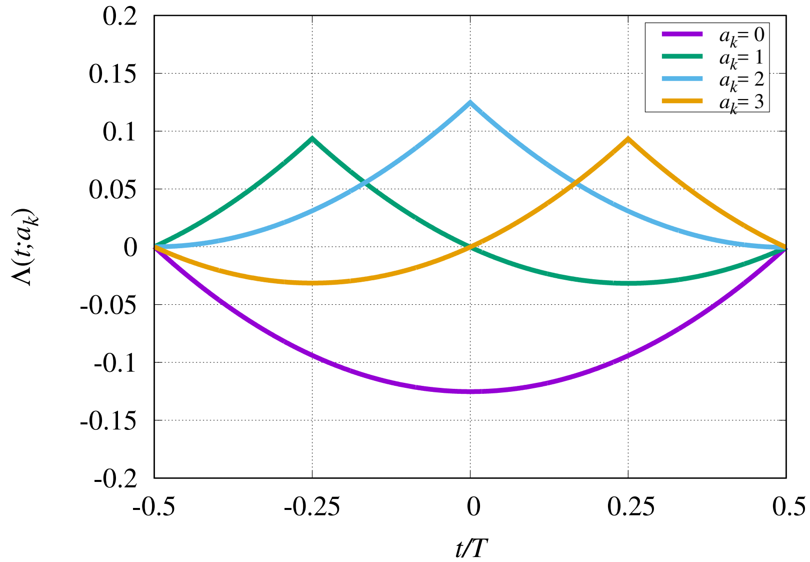

Figure 4.2: Function $\Lambda(t;a_k)$ for different values of a_k in the case $\mathrm{SF}=2$.

A closed-form expression of the power spectral density $W_s(f)$ of a signal that can be expressed in the form (4.4) exists [56]. It is composed of a continuous part $W_c(f)$ and a discrete part $W_\delta(f)$ made of a modulated Dirac delta train

$$W_s(f) = W_c(f) + W_\delta(f)$$

where

$$W_c(f) = \frac{1}{T}\left[\frac{1}{N}\sum_{a_k}|\Xi(f;a_k)|^2 - \left|\frac{1}{N}\sum_{a_k}\Xi(f;a_k)\right|^2\right]$$

and

$$W_\delta(f) = \frac{1}{N^2T^2}\sum_{n=-\infty}^{\infty}\left|\sum_i \Xi(\frac{n}{T};a_i)\right|^2 \delta(f-\frac{n}{T})$$

having denoted by $\Xi(f;a_k)$ the Fourier transform of $\xi(t;a_k)$ whose closed-form expression is

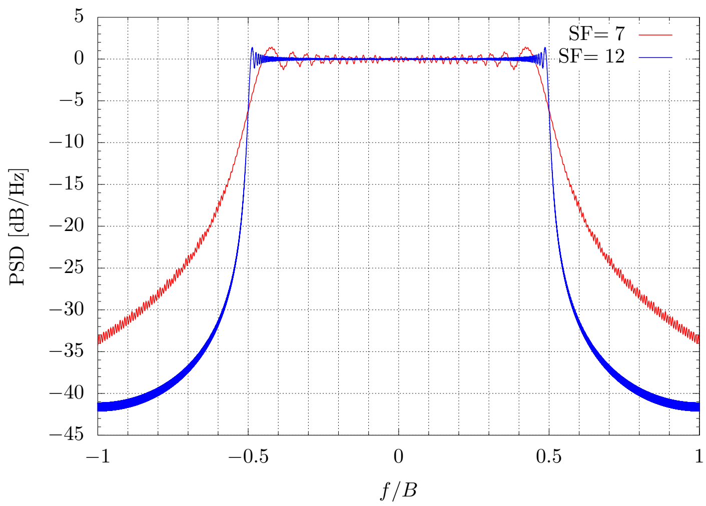

Figure 4.3: Continuous part $W_c(f)$ of the power spectral density of LoRa signals for SF $= 7$ and SF $= 12$.

$$
\begin{aligned}
\Xi(f;a_k) \quad = \sqrt{\tfrac{E_\mathrm{s}T}{N}} \quad & e^{j2\pi B\left(\frac{3T}{8}-\frac{T}{2}\left(\frac{a_k}{N}+\left(+\frac{a_k}{N}-1+\frac{f}{B}\right)^2\right)\right)} \\
& \cdot\left\{Z\left[\sqrt{2N}\left(+\frac{1}{2}-\frac{f}{B}\right)\right]-Z\left[\sqrt{2N}\left(-\frac{a_k}{N}+\frac{1}{2}-\frac{f}{B}\right)\right]\right\} \\
& +\sqrt{\frac{E_\mathrm{s}T}{N}}e^{j2\pi B\left(-\frac{T}{8}+\frac{T}{2}\left(\frac{a_k}{N}+\left(\frac{a_k}{N}+\frac{f}{B}\right)^2\right)\right)} \\
& \cdot\left\{Z\left[\sqrt{2N}\left(-\frac{a_k}{N}+\frac{1}{2}-\frac{f}{B}\right)\right]-Z\left[\sqrt{2N}\left(-\frac{1}{2}-\frac{f}{B}\right)\right]\right\}
\end{aligned}
$$

where $Z(\cdot) = C(\cdot) + jS(\cdot)$, $C(x) = \int_0^x \cos(\frac{\pi}{2}y^2)dy$ and $S(x) = \int_0^x \sin(\frac{\pi}{2}y^2)dy$ are the Fresnel integrals [57]. Fig. 4.3 reports the continuous part $W_c(f)$ of the power spectral density of LoRa signals for SF $= 7$ and 12. From this figure, we can see that a significant portion of the power is in the frequency range $[-\frac{B}{2}, \frac{B}{2}]$ (thus the bandwidth of the corresponding passband signal is B).

Another empirical evidence of property 4, i.e., that B is a suitable bandwidth definition for LoRa signals, is provided by the following experiment. We generated signal $s(t)$ according to (4.1) and then sampled it with N_s samples per symbol time. The sampling frequency is thus $F_s = \frac{N_s}{T}$. Samples $\{s(kT/N_s)\}$ are then interpolated by using the Whittaker–Shannon interpolation formula [58], thus obtaining the interpolated signal $\bar{s}(t)$. In Figs. 4.4 we report, for the cases SF $= 7$ and SF $= 12$, the normalized MSE

$$\varepsilon^2 = \frac{1}{2E_s}\mathrm{E}\left\{\int_{-T/2}^{T/2} |s(t) - \bar{s}(t)|^2 \, dt\right\}$$

where $\mathrm{E}\{\cdot\}$ denotes expectation, as a function of N_s/N. It can be observed that the error is negligible when $N_s \geq N$. Thus, a sampling frequency $F_s \geq \frac{N}{T}$ is sufficient to ensure the reconstruction of the original signal from its samples with a very good approximation. By using (4.3), we obtain that the sampling frequency must be such that

$$F_s \geq \frac{N}{T} = B \,. \tag{4.5}$$

According to the sampling theorem, we know that signal $s(t)$ can be reconstructed from its samples taken at a frequency F_s which is twice its bandwidth. Hence, from (4.5) we infer that a good estimate of the bandwidth of $s(t)$ is $B/2$, and thus B is a good estimate of the bandwidth of the corresponding passband signal.

From the observation of Fig. 4.1, we can easily understand that we may express

$$\Gamma(t;a_k) = \Gamma(t;0) + \Phi(t;a_k)$$

i.e., as a first contribution which is the value of $\Gamma(t;a_k)$ corresponding to symbol $a_k = 0$, thus common to all terms, plus a second term which depends on a_k and can be expressed as

$$\Phi(t;a_k) = \begin{cases} -\frac{a_k}{N} + 1 & \text{for } -\frac{T}{2} \leq t \leq -\frac{T}{2} + \frac{a_k T}{N} \\ -\frac{a_k}{N} & \text{for } -\frac{T}{2} + \frac{a_k T}{N} < t \leq \frac{T}{2} \end{cases} . \tag{4.6}$$

$\Phi(t;a_k)$ is thus a piecewise constant and is shown in Fig. 4.5 for different values of a_k in the case of SF $= 2$. Hence, the complex envelope of a LoRa signal in the generic interval $[kT - T/2, kT + T/2]$ (and thus the slice of signal we called $\xi(t - kT;a_k)$) can be equivalently expressed as

$$\xi(t - kT;a_k) = \xi(t - kT;0) \exp\left\{ j2\pi B \int_{kT-T/2}^{t} \Phi(\tau - kT;a_k) \, d\tau \right\}$$

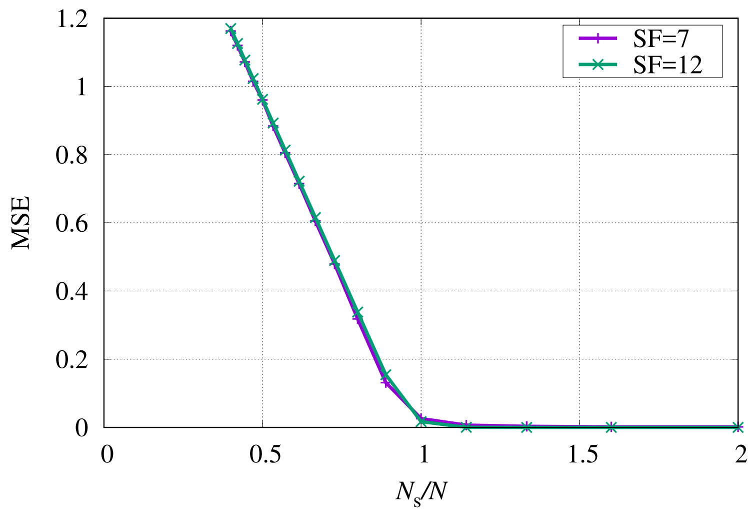

Figure 4.4: Normalized mean square error between signals $s(t)$ and $\bar{s}(t)$ versus N_s for $\mathrm{SF} = 7$ and 12.

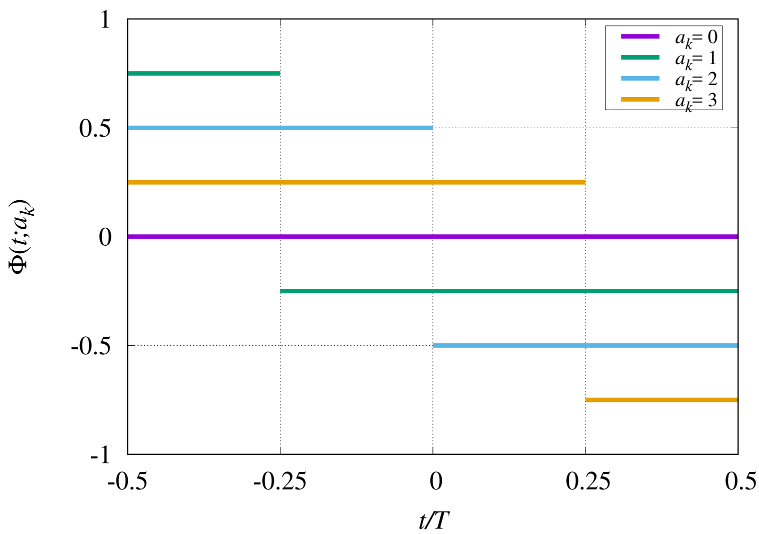

Figure 4.5: Function $\Phi(t;a_k)$ for different values of a_k in the case $\mathrm{SF} = 2$.

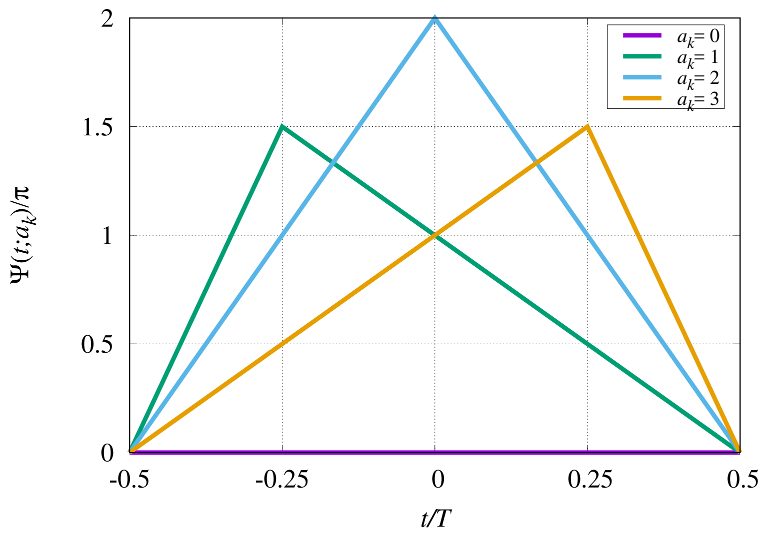

Figure 4.6: Function $\Psi(t;a_k)$ for different values of a_k in the case $\mathrm{SF}=2$.

where

$$\xi(t-kT;0)=\sqrt{\frac{2E_\mathrm{s}}{T}}\exp\left\{j2\pi B\int_{kT-T/2}^{t}\Gamma(\tau-kT;0)\,d\tau\right\} \tag{4.7}$$

is the slice of signal corresponding to $a_k=0$ and is a term whose phase quadratically depends on t (see Fig. 4.2). This is thus an up-chirp signal. We can define

$$\Psi(t-kT;a_k)=2\pi B\int_{kT-T/2}^{t}\Phi(\tau-kT;a_k)\,d\tau$$

obtaining

$$\xi(t-kT;a_k)=\xi(t-kT;0)\exp\{j\Psi(t-kT;a_k)\}\,.$$

The shape of $\Psi(t;a_k)$ is shown in Fig. 4.6 for $SF=2$.

Let us consider again the generic interval $[kT-T/2,kT+T/2]$. The slices $\xi(t-kT;a_k)$ corresponding to different symbols a_k are not orthogonal. This can be simply verified by computing the $N\times N$ matrix $\mathbf{A}$ whose elements are defined as

$$A_{i,\ell}=\frac{T}{2E_\mathrm{s}}\int_{kT-T/2}^{kT+T/2}\xi(t-kT;a_k=i)\xi^*(t-kT;a_k=\ell)\,dt\,.$$

Table 4.1: Normalized distance $\frac{1}{N}\|\mathbf{A}-\mathbf{I}\|_{\mathrm{F}}$ for different values of SF.

SF	$\frac{1}{N}\|\mathbf{A}-\mathbf{I}\|_{\mathrm{F}}$
2	$2.1 \cdot 10^{-1}$
3	$1.3 \cdot 10^{-1}$
4	$7.8 \cdot 10^{-2}$
5	$4.6 \cdot 10^{-2}$
6	$2.7 \cdot 10^{-2}$
7	$1.6 \cdot 10^{-2}$
8	$9.4 \cdot 10^{-3}$
9	$5.5 \cdot 10^{-3}$
10	$3.2 \cdot 10^{-3}$
11	$1.9 \cdot 10^{-3}$
12	$1.1 \cdot 10^{-3}$

Each value $A_{i,\ell}$ represents the correlation between the signal corresponding to the symbol $a_k = i$ and that corresponding to the symbol $a_k = \ell$. If the slices $\xi(t-kT;a_k)$ were orthogonal, $\mathbf{A}$ would be the identity matrix. So, in order to understand how far is this matrix from the identity one, we computed the normalized distance $\frac{1}{N}\|\mathbf{A}-\mathbf{I}\|_{\mathrm{F}}$ where $\mathbf{I}$ is the $N \times N$ identity matrix and $\|\cdot\|_{\mathrm{F}}$ is the Frobenius norm. The values are reported in Table 4.1 for different values of SF. We may thus conclude that the slices $\xi(t-kT;a_k)$ are not strictly orthogonal but can be approximated as such.

We said that signal $s(t)$ has (approximately) a bandwidth $B/2$. It can be thus reconstructed from its samples when using a sampling frequency $F_s = B = N/T$. Without loss of generality, we can consider the interval $[-T/2, T/2]$ and thus the transmission of symbol a_0. By sampling the signal $t = \ell T/N$, the N samples of the complex envelope are

$$\xi\left(\frac{\ell T}{N};a_0\right) = \xi\left(\frac{\ell T}{N};a_0=0\right)\exp\left\{j\Psi\left(\frac{\ell T}{N};a_0\right)\right\}, \quad \ell = -\frac{N}{2}, -\frac{N}{2}+1, \ldots 0, \ldots, \frac{N}{2}-1.$$

By unwrapping the phase $\Psi\left(\frac{\ell T}{N};a_0\right)$, it can be easily verified that

$$\exp\left\{j\Psi\left(\frac{\ell T}{N};a_0\right)\right\}=\exp\left\{-j\frac{2\pi}{N}a_0\left(\ell+\frac{N}{2}\right)\right\},\quad \ell=-\frac{N}{2},-\frac{N}{2}+1,\dots 0,\dots,\frac{N}{2}-1.$$

and thus

$$\xi\left(\frac{\ell T}{N};a_0\right)=\xi\left(\frac{\ell T}{N};a_0=0\right)\exp\left\{-j\frac{2\pi}{N}a_0\left(\ell+\frac{N}{2}\right)\right\},\quad \ell=-\frac{N}{2},-\frac{N}{2}+1,\dots 0,\dots,\frac{N}{2}-1$$

or, equivalently,

$$\xi_n(a_0)=\xi_n(a_0=0)\exp\left\{-j\frac{2\pi}{N}a_0 n\right\},\quad n=0,1,\dots,N-1 \tag{4.8}$$

having defined $n=\ell+\frac{N}{2}$ and

$$\xi_n(a_0) \quad = \quad \xi\left(\frac{n-\frac{N}{2}T}{N};a_0\right).$$

In other words, we can write the samples as the product of an up-chirp signal, common to all signals, and a term whose phase is linearly decreasing with a slope depending on the transmitted symbol. These discrete-time samples are, this time, orthogonal. In fact

$$\sum_{n=0}^{N-1}\xi_n(a_0=i)\xi_n^*(a_0=\ell)=\begin{cases}N & i=\ell\\ 0 & i\neq\ell\end{cases}.$$

This property will be used later. It is important to notice that if we sample with a lower or higher sample frequency, this property no more holds, i.e., we can still write the samples as the product of an up-chirp signal, common to all signals, and a second term depending on the transmitted symbol, but this time the phase of this second term is no more linearly decreasing.

4.2 Receiver design

4.2.1 Detection over an AWGN channel

Let us assume that an uncoded LoRa signal is transmitted over an AWGN channel and that ideal synchronization has been performed (synchronization issues will be discussed in Section 4.2.3). Without loss of generality, since the modulation is memoryless, as discussed in the previous section, we can consider the interval $[-T/2, T/2]$ focusing on detection of symbol a_0 only. The complex envelope of the received signal can thus be expressed as

$$r(t) = \xi(t; a_0) + w(t)$$

where $w(t)$ is the complex envelope of the additive white Gaussian noise. $w(t)$ is a complex Gaussian noise process with independent real and imaginary components having zero mean and power spectral density N_0.

From a conceptual point of view, optimal detection of LoRa signals can be performed through the following MAP detection strategy [59][1]

$$\hat{a}_0 = \operatorname*{argmax}_{a_0} \Re\{z(a_0)\} \tag{4.9}$$

having defined

$$z(a_0) = \int_{-T/2}^{T/2} r(t)\xi^*(t; a_0)\, dt$$

i.e., $z(a_0)$ is obtained by sampling the received signal $r(t)$ filtered through a filter matched to $\xi(t; a_0)$. We can thus conclude that a sufficient statistic can be obtained through a bank of $N = 2^{\mathrm{SF}}$ filters matched to all possible waveforms waveforms $\xi(t; a_0)$.

Although this receiver is quite simple from a conceptual point of view, it can hardly be implemented when N grows. Let us consider a digital implementation of the bank of N matched filters. In practical receivers, an approximated set of sufficient statistics is obtained through the technique described in [25]. It is assumed that

[1] This detection strategy has been obtained by exploiting the fact that $\xi(t; a_0)$ has a constant envelope.

the LoRa low-pass equivalent is band-limited with bandwidth $B/2$—although this is not strictly true as discussed in the previous section. The approximated statistics can be obtained by sampling the received signal prefiltered by means of an ideal analog lowpass filter having bandwidth $B/2$. The use of an ideal filter ensures that the noise samples are i.i.d. complex Gaussian random variables with independent components. As discussed in the previous section, we need at least N samples to represent the transmitted signal in the interval $[-T/2, T/2]$. The complexity related to the implementation of N matched filters is thus proportional to N^2.

A significant complexity reduction can be obtained by exploiting (4.8). In fact, we can express the received samples as

$$r_n = \xi_n(a_0 = 0)e^{-j\frac{2\pi}{N}a_0 n} + w_n$$

where w_n are additive white Gaussian noise samples [25]. We can thus remove the up-chirp signal by computing

$$y_n = r_n^* \xi_n(a_0 = 0) = e^{j\frac{2\pi}{N}a_0 n} + w_n'$$

where w_n' are still additive white Gaussian noise samples since the up-chirp signal has a constant amplitude and does not modify the noise statistics. The optimal MAP detection strategy based on these samples can be expressed as

$$\hat{a}_0 = \operatorname*{argmax}_{a_0} \Re\left\{\sum_{n=0}^{N-1} y_n e^{-j\frac{2\pi}{N}a_0 n}\right\}. \tag{4.10}$$

Looking at (4.10), we can recognize that the strategy can be expressed as

$$\hat{a}_0 = \operatorname*{argmax}_{k} \Re\{Y_k\}$$

having defined

$$Y_k = \sum_{n=0}^{N-1} y_n e^{-j\frac{2\pi}{N}kn}$$

as the Discrete Fourier Transform (DFT) of samples y_n. It can be thus efficiently computed through the Fast Fourier Transform (FFT) with complexity $N\log_2 N = N \cdot \mathrm{SF}$.

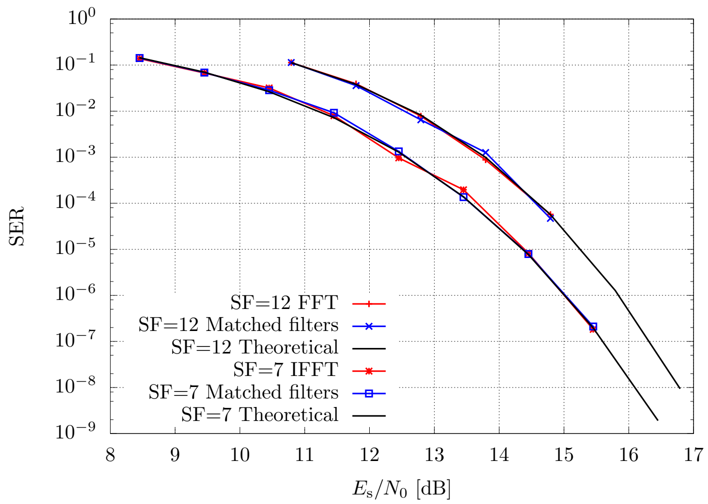

Figure 4.7: SER for strategies (4.9) and (4.10).

The error probability of strategy (4.10) is known in an analytical form. In fact, since the discrete-time waveforms are orthogonal, the symbol error probability is exactly the same of any other orthogonal modulation scheme and reads [59]

$$P_S = 1 - \frac{1}{\sqrt{2\pi}} \int_{-\infty}^{+\infty} \exp\left\{-\frac{x^2}{2}\right\} \left[1 - \mathrm{Q}\left(x + \sqrt{2\frac{E_s}{N_0}}\right)\right]^{N-1} dx \qquad (4.11)$$

where $\mathrm{Q}(\cdot)$ is the Gaussian Q function.

As said, strategies (4.9) and (4.10) are only approximately equivalent. In fact, strategy (4.10) has been obtained under the approximated assumption that LoRa signal (4.1) has a limited bandwidth $B/2$. Since this is not strictly true, it is interesting to evaluate the performance loss related to this approximation. In Fig. 4.7 we report the Symbol Error Rate (SER) versus E_s/N_0 of both strategies in the case of an uncoded transmission. For strategy (4.10) we also report the theoretical curve (4.11). The cases of $\mathrm{SF} = 7$ and 12 have been considered. It may be observed that both strategies have practically the same performance. We can conclude that the approximation that allows to obtain strategy (4.10) is very good.

4.2.2 Noncoherent detection

Detection strategies (4.9) and (4.10) have been obtained under the assumption of ideal synchronization. We will now consider phase noise and the related performance loss it produces on strategies (4.9) and (4.10).

The optimal detection strategy in the presence of phase noise will depend on the channel coherence time. When the channel coherence time is long enough, we can exploit its correlation to design a receiver with memory with a negligible performance loss with respect to the case of ideal synchronization [60]. On the other end, when the channel phase is assumed to change independently every symbol interval, the system is again memoryless and the receiver will have the lowest possible complexity. It can be easily shown that when the channel phase is assumed uniformly distributed and to change independently every symbol interval, the strategies (4.9) and (4.10) become

$$\hat{a}_0 = \underset{a_0}{\operatorname{argmax}} |z(a_0)| \tag{4.12}$$

and

$$\hat{a}_0 = \underset{a_0}{\operatorname{argmax}} \left| \sum_{n=0}^{N-1} y_n e^{-j\frac{2\pi}{N}a_0 n} \right| . \tag{4.13}$$

These kinds of strategies are called “noncoherent” in the literature. In particular, we will consider strategy (4.13) only, since it can be implemented through the FFT. Fig. 4.8 reports, for $SF = 7$ and 12, the SER performance of strategy (4.10) under the assumption of perfect knowledge of the channel phase (curves labeled “coherent”) and that of strategy (4.13) under the assumption that the channel phase is unknown, constant over a symbol interval, and changing independently every symbol interval. It can be observed that the performance loss of this noncoherent strategy is lower than 0.5 dB. Thus, we believe that it is not worth investigating the possibility to exploit the phase noise correlation in case of a longer coherence time.

4.2.3 Properties of LoRa signals to be exploited for synchronization

In this section, we will discuss on synchronization of LoRa signals. In particular, we will see which properties of LoRa signals can be exploited to perform frame,

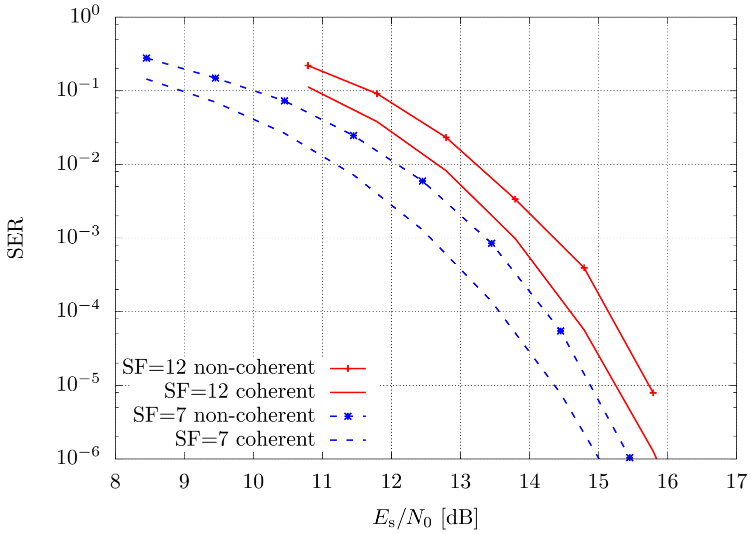

Figure 4.8: SER comparison between strategies (4.10) and (4.13).

frequency, and timing synchronization. In Section 4.2.6, we will describe the entire synchronization procedure.

The preamble of a LoRa packet is characterized by 8 consecutive up-chirps, two “special” modulated symbols, and 2.25 down-chirps. For the sake of clarity, we reported in Fig. 4.9 the value of the instantaneous frequency $\Gamma(t)$ of these 12.25 preamble symbols. Let us consider an up-chirp signal in the reference interval $[-T/2, T/2]$. It can be expressed in closed form as (see (4.7))

$$
\begin{aligned}
\xi(t;0) &= \sqrt{\frac{2E_s}{T}} \exp\left\{ j2\pi B \int_{kT-T/2}^{t} \Gamma(\tau;0)\, d\tau \right\} \\
&= \sqrt{\frac{2E_s}{T}} \exp\left\{ j2\pi B \left(\frac{t^2}{2T} - \frac{T}{8} \right) \right\}.
\end{aligned}
$$

Let us now assume that a train of up-chirp signals experiences a delay τ (we will assume $0 \leq \tau \leq T$) and is affected by a frequency uncertainty ν (due to the uncertainty on the nominal frequency of the transmitted signal and the Doppler shift)

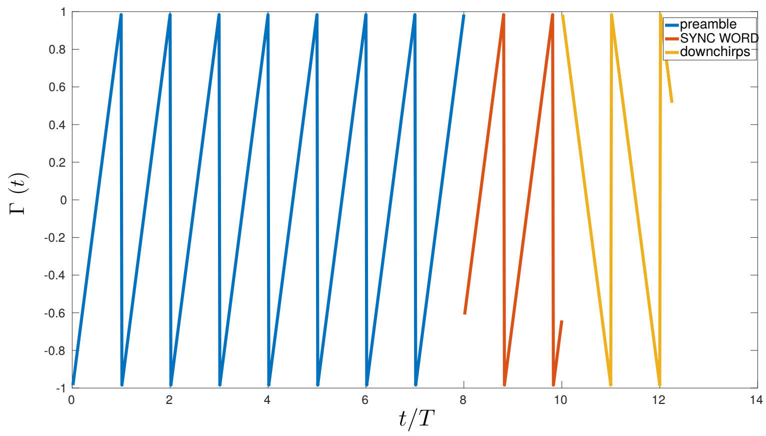

Figure 4.9: Instantaneous frequency $\Gamma(t)$ for the sequence of preamble symbols in LoRaWAN.

and a phase shift θ_0, in addition to the AWGN.[2] The complex envelope of the received signal can be thus expressed as

$$r(t) = \beta \sum_k \xi(t - kT - \tau; 0) e^{j(2\pi\nu t + \theta_0)} + w(t)$$

where β is the attenuation due to propagation and $w(t)$ is a complex Gaussian AWGN process.

Due to the presence of the frequency uncertainty ν, a discrete-time sufficient statistic can still be obtained with the same technique already described in Section 4.2.1, but N samples per symbol are no more sufficient. We will thus need to extract N_o samples, with $N_\mathrm{o} > N$, after the analog prefilter. These samples r_n are then multiplied by the complex conjugate of the samples of the original train of up-chirp signals (dechirping operation). This multiplication does not change the noise statistics. The received samples after dechirping in the reference symbol interval $[-T/2, T/2]$ can be expressed as

$$y_n = s_n + w_n\,, \quad n = -\frac{N_\mathrm{o}}{2}, -\frac{N_\mathrm{o}}{2}+1, \ldots, \frac{N_\mathrm{o}}{2}-1 \tag{4.14}$$

[2]We will consider the effect of the Doppler rate α later.

where w_n is a discrete-time complex white Gaussian noise process and samples s_n can be expressed as

$$s_n = \begin{cases} \gamma e^{j\theta_1} \exp\left\{ j2\pi \left(B + \nu - B\frac{\tau}{T}\right) n \frac{T}{N_o} \right\} & -\frac{N_o}{2} \leq n < -\frac{N_o}{2} + N_1 \\ \gamma e^{j\theta_2} \exp\left\{ j2\pi \left(\nu - B\frac{\tau}{T}\right) n \frac{T}{N_o} \right\} & -\frac{N_o}{2} + N_1 \leq n < \frac{N_o}{2} \end{cases}$$

where γ is a proper amplitude, taking into account the amplitude of the transmitted signal, the channel attenuation and the amplitude of the up-chirp signal used for dechirping, and having defined $N_1 = \lfloor N_o \frac{\tau}{T} \rfloor$, where $\lfloor x \rfloor$ denotes the largest integer lower than or equal to x, and

$$\begin{aligned} \theta_1 &= 2\pi B \left(\frac{T}{2} + \frac{\tau^2}{2T} - \tau \right) + \theta_0 \\ \theta_2 &= 2\pi B \frac{\tau^2}{2T} + \theta_0 \,. \end{aligned}$$

The computation of the Fourier transform of sequence s_n, $n = -\frac{N_o}{2}, -\frac{N_o}{2}+1, \ldots, \frac{N_o}{2} - 1$, will exhibit a maximum of amplitude $\max(N_1, N_o - N_1)$ either at frequency $\left(\nu - B\frac{\tau}{T}\right)$ or at frequency $\left(B + \nu - B\frac{\tau}{T}\right)$. This maximum can be identified by using the Rife & Boorstyn algorithm [61] which is based on two steps. A *coarse search* is first performed by computing some samples of the Fourier transform through the FFT and looking for the maximum sample. An interpolation is then performed around this maximum samples to refine the search (*fine search* step).

If we repeat the same operations for the down-chirp signal (this time using the down-chirp signal to perform dechirping) we obtain again a maximum of amplitude $\max(N_1, N_o - N_1)$ but this time either at frequency $\left(\nu + B\frac{\tau}{T}\right)$ or at frequency $\left(B + \nu + B\frac{\tau}{T}\right)$. In the next section we will see how to exploit this property to perform frame, frequency, and timing estimate.

When a Doppler rate α is also present, we observe an uncompensated frequency offset ν that varies linearly with time at a slope α. However, considering the values of α at stake, we can approximate this linear variation with a staircase, i.e., constant over a symbol and changing from symbol to symbol. So the frequency corresponding to the maximum amplitude of the Fourier transform, when performed on consecutive symbols, will increase or decrease linearly (depending on the sign of α). We have to take this into account when performing synchronization and detection.

4.2.4 Estimation of the frequency peaks

The estimation of the above-mentioned frequency peaks is a challenging task. In fact, the energy of a single sample is far lower than the noise power, leading to a high number of outliers in the estimation process that could degrade the performance. Because of this, algorithms for frequency estimation working in the time domain, such as that by Mengali & Morelli [62] which has, for high SNR values, a performance close to that of the Rife & Boorstyn algorithm but with a lower complexity, become useless since they start converging only at very high SNR values.

We investigated the convergence properties of the Rife & Boorstyn algorithm. In Fig. 4.10, we report the mean square estimation error, normalized to N_o/NT, versus the SNR for the Rife & Boorstyn algorithm applied to the samples of a single symbol (thus to a total number of samples N_o) for the case with $SF = 12$. We chose $N_o = 2N$ for the reasons explained later. It can be observed that it approaches the Modified Cramér-Rao Lower Bound (MCRLB) [63], also reported for convenience, for high values of E_s/N_0 only. For lower values, a significant number of outliers, is present. These outliers degrade the performance.

A simple approach to reduce the occurrence of the outliers is the following: instead of considering the FFT of a block of samples related to a single symbol, we compute the magnitude of the transform of two symbols and sum them together. In this way, peaks due to noise are averaged out and signal peaks will sum constructively. The fine estimation is made through zero-padding before FFT. As shown in Fig. 4.10, this is not an optimal approach since the estimator's performance is farther from the MCRLB. However, convergence is reached at lower SNR values.

A similar procedure of computing the magnitude of the transform of more symbols and sum them together can be also employed when searching for the preamble to perform frame synchronization. The difference is that at this stage the receiver does not need the fine estimation step since we are only interested in revealing the presence of the preamble pattern.

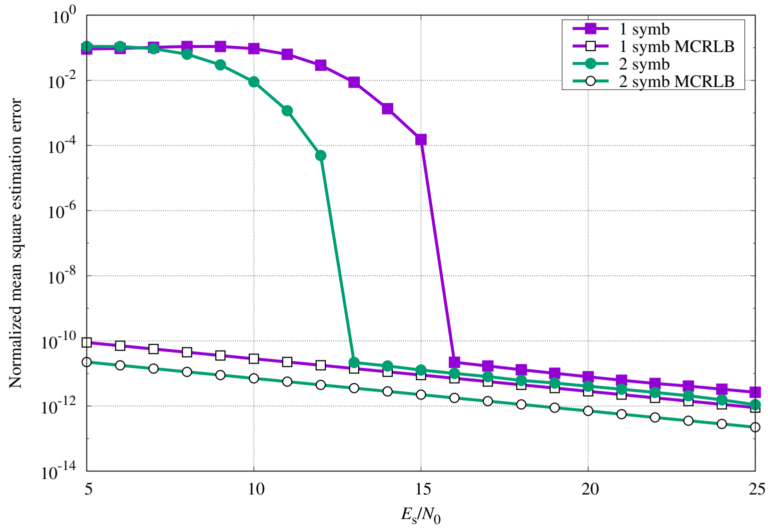

Figure 4.10: Normalized mean square estimation error for the adopted algorithms used for the identification of the frequency peaks. The corresponding MCRLB is also reported for comparison.

4.2.5 Doppler rate estimation

The Doppler rate entailed by the satellite motion along its orbit turns out to be a very detrimental impairment, when the LoRa modulation is employed on a satellite link. Figs.4.11(a)-4.11(b) outline the amount of Doppler shift and Doppler rate from satellite projection on Earth surface. Their computation is based on the work in [64]. As can be noticed, maximum values of Doppler shift and Doppler rate are bounded by (approximately) 20 kHz and 245 Hz/s, respectively. The frequency shift due to the Doppler effect has to be cumulated with that coming from the frequency instability of the employed oscillators, and can be estimated as described in the previous section. On the contrary, the Doppler frequency shift variation, i.e., the Doppler rate, is peculiar of the satellite link scenario. The main problem here is that the LoRa modulation is basically a frequency modulation and thus a linear change in the frequency can strongly affect its performance. Moreover, the modulation and the preamble were not designed to deal with this impairment.

The maximum value of the Doppler rate entails a frequency deviation, from one symbol to the next, which is comparable to the frequency separation between two adjacent symbols, for the highest values of SF. In fact, for SF = 12 the separation is approximately 30 Hz (for SF = 11 it is approximately 61 Hz). Since the frequency variation due to the Doppler rate from one received symbol to the next can be up to 8 Hz, this means that, for SF = 12, the symbol sequence can be shifted by one position every 4 received symbols.

In the presence of Doppler rate, the received samples (4.14) can be expressed as

$$z_n = s_n \exp\{j2\pi\alpha k^2 T_\mathrm{s}^2\} + w_n, \tag{4.15}$$

where α represents the Doppler rate and $T_\mathrm{s} = T/N_\mathrm{o}$ the sampling time. The system sensitivity to Doppler rate can be evaluated through simulations. In the case SF = 10 and 12 and a packet of 45 symbols, without preamble, in Fig.4.12 we report the PER, versus the signal-to-noise ratio, for different values of the uncompensated Doppler rate. For SF = 12, it can be noticed that a significant penalty is already observed for a Doppler rate around 6 Hz/s, whereas the PER is equal to 1 when the Doppler rate exceeds 10 Hz/s (in fact, simple calculations show that in this case a Doppler

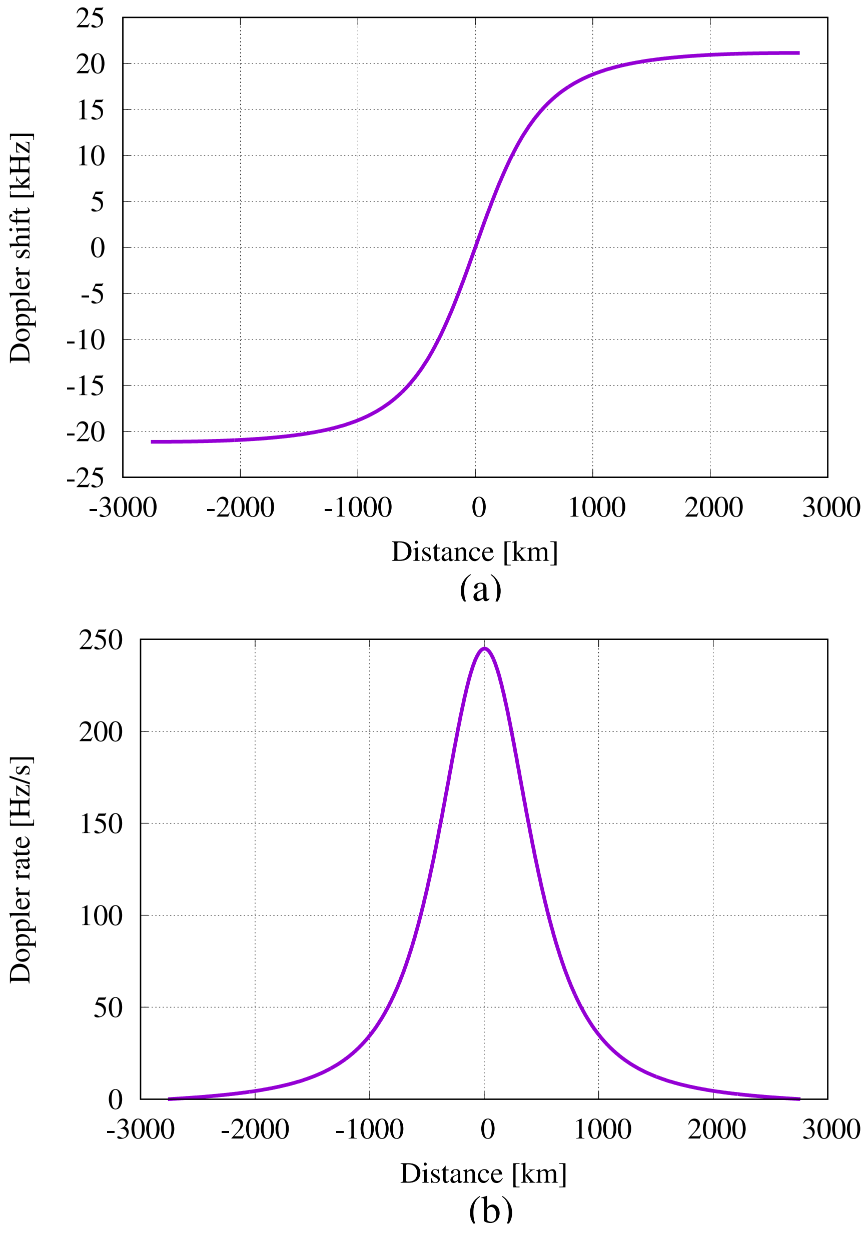

Figure 4.11: a) Doppler shift and b) Doppler rate as a function of the distance from the satellite projection on the Earth surface.

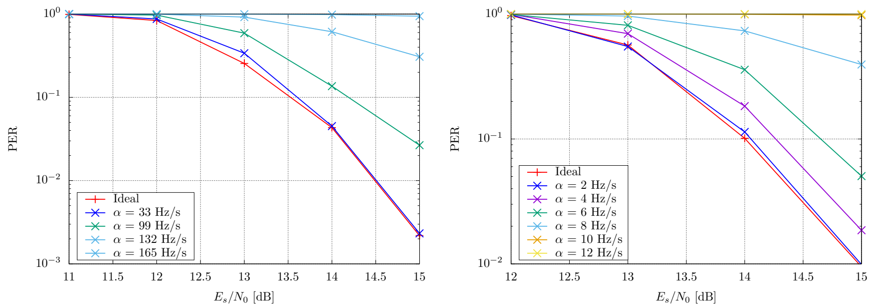

Figure 4.12: PER performance in the presence of Doppler rate, with perfect compensation of timing and frequency offset, for SF = 10 on the left and SF = 12 on the right.

rate ~11 Hz/s yields a symbol shift by the end of the packet, even in the absence of noise). Hence, it is required to estimate the Doppler rate value with an accuracy of a few Hz/s. In the case SF = 10 instead, higher values of Doppler rate are required to worsen the performance.

There exist several algorithms for data-aided Doppler rate estimation. One of the most effective algorithms is that proposed in [65], and can be directly applied to the received signal once modulation and chirping have been removed, and timing and frequency offset have been compensated for. However, when applied to our scenario, it does not provide the required accuracy. We investigated the performance of the algorithm in [65], applied in three different ways, all exploiting the received samples corresponding to N_e =10 preamble symbols (8 up-chirp symbols and the 2 following "special" known symbols). The first approach (alg. #1), consisted in employing all 10 symbols together and with optimized algorithm parameters (specifically, $L = 256$, see [65]). In the second algorithm we tested (alg. #2), we applied the algorithm 10 times to the samples of each symbol and then we averaged over the 10 estimates. In the third approach, we averaged over 10 estimates computed by taking one sample every 10 from the whole sequence of samples corresponding to 10 symbols (alg. #3). Besides, we simulated an algorithm based on the Rife-Boorstyn technique to obtain the estimates of the peak position on each symbol interval, and processed these different estimates (alg. #4). In other words, in this case we estimate the Doppler rate by observing the position of the frequency peaks throughout the 10 preamble symbols. The peak values are then processed in order to find the linear regression which represents the frequency increment due to Doppler rate. Nevertheless, the few available data suffer by a high incidence of outliers, which are partly due to the low SNR, but also to the residual timing compensation error. A feasible solution, thus, is to further process the preamble samples, in order to reduce the impact of such outliers on the estimate. Basically, the estimation is performed on the 10 symbols (the down-chirps cannot be used because the unavoidable imperfect timing compensation leads to a phase shift with respect to the up-chirped symbols, which typically worsen the estimation), which are used in pairs to compute many different Doppler rate estimates, essentially two-point linear regressions, instead of computing a single linear regression estimate using all 10 symbols; an average over these estimates turns out to have a better performance, since the effect of the outliers is more likely to be averaged out. Fig. 4.13 outlines the results in terms of square root of the Mean Square Estimation Error (MSEE), normalized to the sampling frequency, obtained by averaging over 10000 trials per SNR value, and assuming perfect timing and frequency offset compensation. The MCRLB is also reported for convenience. It is worth specifying that results do not change with the amount of the considered Doppler rate value. We can observe that, although algorithms 1 and 3 are able to reach the MCRLB, they start converging for very high values of the signal-to-noise ratio. On the contrary, algorithm 4 remains quite far from the MCRLB but its convergence threshold is much lower, around ~15 dB. Moreover, we should consider that, actually, algorithms #1 and #3 turn out to be unreliable under non-ideal conditions, since the phase jumps between adjacent symbols, due to imperfect timing compensation, severely affect their performance.

Finally, Fig. 4.14 shows the performance of the algorithm #4, for increasing number of symbols N_e used for the estimation compared with the required minimum value of the accuracy (~6 Hz/s, which was previously identified as a critical value). The idea here is to use the decisions to improve the estimate accuracy in a decision-directed mode. Since, in any case, the performance of the estimators and the minimum value

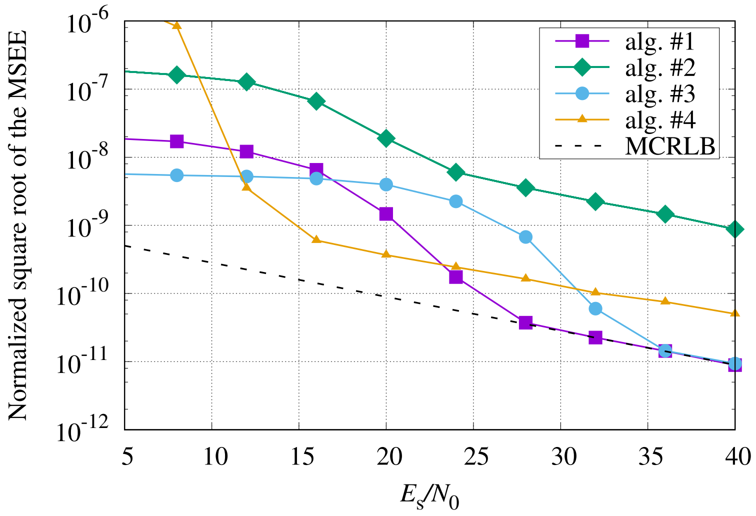

Figure 4.13: Normalized square root of the MSEE for the four considered algorithms. The MCRLB is also reported.

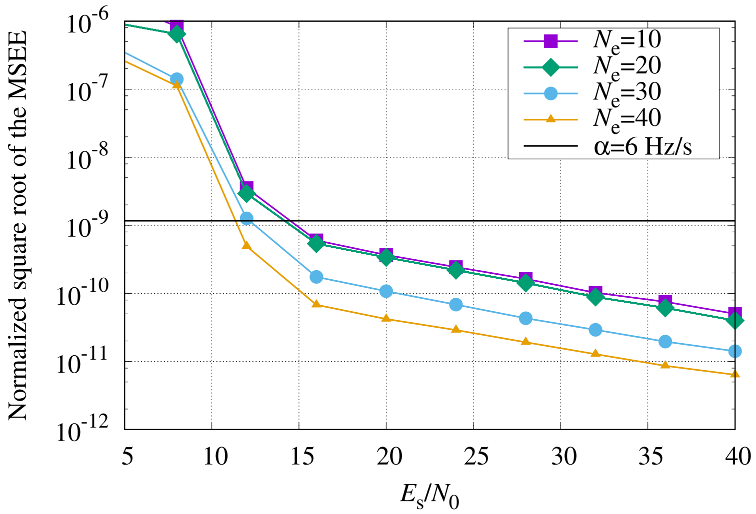

Figure 4.14: Normalized square root of the MSEE for increasing number of symbols.

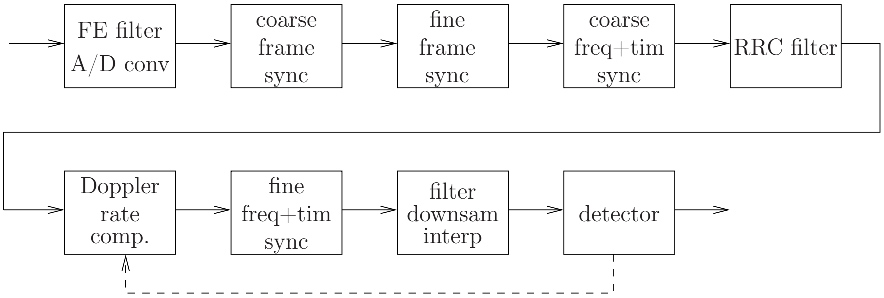

Figure 4.15: Overall receiver.

of the accuracy have the same order of magnitude, especially around 15 dB, it turns out that the Doppler rate estimation is a really challenging task.

4.2.6 Overall receiver

The overall receiver, comprising the synchronization and detection procedure, is shown in Fig. 4.15.

As previously mentioned, the received analog signal is first filtered through a front end prefilter and then sampled at frequency $F_s = \frac{N_o}{T} \geq B + 2\nu_{\max}$, where $\nu_{\max}$ is the maximum value of the frequency uncertainty. Considering the value of $\nu_{\max}$ for a LEO satellite, the bandwidth of the analog prefilter will be much larger than that of the transmitted signal (and we will also need to sample with $N_o \simeq 2N$ samples). A lot of noise will thus affect the received samples and this will have an impact on the performance of the synchronization algorithms that have to be performed in a coarse and a fine step. First, we need to detect the presence of a transmitted packet through the search of the known preamble. A coarse search for the preamble must be performed and we will assume a continuous operation mode. The search is performed by considering blocks of non-overlapping N_o samples, performing dechirping on them, and processing them through FFT. Then we store the location of the maximum value of the function obtained by summing the magnitude of the FFTs of two consecutive blocks. Then, we move forward of one symbol and repeat this operation. In practice, pairs of blocks are considered, with an overlap of one block between two consecutive pairs. When the maxima of 7 pairs of blocks are all in the same position on the FFT grid we are in the presence of 8 up-chirps. Two problems arise at this point. As discussed, two peaks at distance B can be observed and, because of the noise, the maximum can "jump" between these peaks. Moreover, the Doppler rate could increasingly shift the maxima throughout the preamble. Hence, instead of looking for 7 consecutive peaks at the exact same position, we relax this constraint by looking for less than 7 consecutive peaks, possibly not exactly at the same position and possibly making "jumps" of B in their position. This is done to reduce the missed detection probability since the false alarm probability is not a problem per sé. In fact, even if we erroneously identify a preamble, the verification of the Cyclic Redundancy Code (CRC) after detection will identify the absence of a valid packet.

The previous step is able to identify the presence of a packet but we will have a significant uncertainty on its beginning. As a consequence, the receiver has to start a fine frame synchronization procedure. The aim of this procedure is to identify its position more precisely, and to reduce the uncertainty on the timing offset. This time, we take blocks of 10 consecutive symbols. Dechirping is performed by multiplying them by the complex conjugate of the first 10 symbols in the preamble. The magnitude of the FFTs of these 10 symbols are computed, then summed, and both position P and amplitude A of the maximum of the result are computed and stored. The window containing these 10 symbols is then shifted of $T/4$ and the same operations performed over another block of 10 symbols, partially overlapped with the previous one. We iterate this procedure around the position returned by the coarse preamble search and keep the P corresponding to the largest stored value of the amplitude A. Now, the starting position of a packet is identified with an uncertainty lower than $T/4$.

We can now perform coarse frequency and timing estimation. The position P obtained in the previous step will provide an estimate of either the frequency $\left(\nu - B\frac{\tau}{T}\right)$ or the frequency $\left(B + \nu - B\frac{\tau}{T}\right)$. By repeating the same operation on the two down-chirp symbols we will obtain an estimate of either the frequency $\left(\nu + B\frac{\tau}{T}\right)$ or the frequency $\left(B + \nu + B\frac{\tau}{T}\right)$. We now have to extract an estimate of both ν and τ, considering the ambiguity caused by the presence of two peaks and also taking into account the cyclic nature of the FFT. Some of the possible pairs of ν and τ will correspond to values outside the allowed ranges. The remaining pairs can be disambiguated through a trial-and-error procedure, that consists in applying the compensation pair to an upchirp block and then verifying if the maximum of its FFT is located in the zero (DC) tone (it is worth noting that it is not necessary to perform a whole FFT processing on the symbol, but rather a processing on the tones around DC only).

After the coarse compensation of timing and frequency offset, a tight filtering can be performed in order to reduce excess noise and improve the performance of the following estimation steps. We used a filter with RRC amplitude and linear phase, with roll-off factor 0.06 and bandwidth B. At this stage, the Doppler rate estimation and compensation is performed.

Fine frequency and timing estimation is then performed. The algorithm is exactly the same used in the coarse step, but this time we take advantage of the suppression of the excess noise and of the Doppler rate compensation. After the estimation, the frequency shift is compensated, while fractional timing compensation and downsampling to N samples can take place at the same time, through interpolation. Now, noncoherent detection can finally be performed, as described in Sec. 4.2.2.

The accuracy of the Doppler rate estimate should allow the detection of the first N_p payload symbols. We can use these N_p symbols to refine the estimate and increase the accuracy. So, we go compensate the Doppler rate with the new estimate, repeat the fine frequency and timing synchronization, repeat the detection and, this time we use the first $2N_p$ symbols to refine the estimate. Thus, we repeat the procedure adding N_p symbols at each iteration until the end of the packet is reached. We used $N_p = 5$ in our simulations.

4.3 Numerical results

We assessed the performance of the overall receiver through computer simulations. We considered the case of absence of interference (the performance in a more realistic scenario where interference takes place is considered in [3]). The results, in terms of PER versus the carrier-to-noise ratio C/N, i.e., the ratio between the signal and the

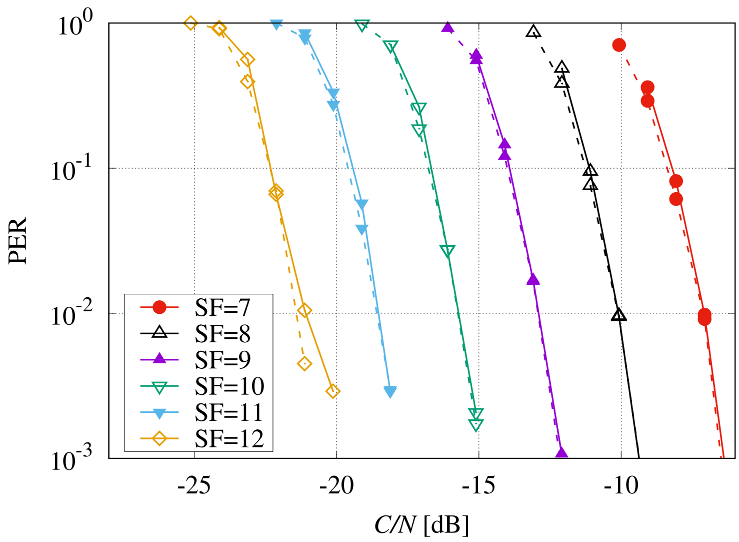

Figure 4.16: PER performance in presence of random impairments (continuous lines), and with perfect estimation and compensation (dashed lines), for $\mathrm{SF} = 7 \div 12$.

noise power, for different values of SF are reported in Fig. 4.16 and compared with that of an ideal receiver which perfectly knows the channel parameters. We considered packets of 50 symbols including the preamble and assumed that Doppler rate and Doppler shift take on the maximum possible values for the considered scenario. As mentioned, when $SF = 12$, the Doppler rate estimation and compensation is necessary (see previous sections for insights), and the penalty due to impairments can be estimated as ~0.3 dB at a PER=10^{-2}. The transmission of a signal with $\mathrm{SF} = 10$ instead can be considered as borderline, since the maximum Doppler rate can induce a symbol shift only after ~40 symbols. However, for values $\mathrm{SF} \leq 10$, it seems better to perform the Doppler rate estimation based on the uncompensated signal, at each iteration of the decision-directed refinement process, rather than performing it on the signal corrected in the previous iteration. This is due to errors in the estimation when there is only the small residual rate left.

4.4 Conclusions

The aim of this chapter was to design a receiver to extend the IoT LoRa networks through LEO satellites in remote areas. We described the LoRa modulation and proposed a design of a receiver that copes with the typical impairments of a LEO satellite link. We saw that, being LoRa a frequency modulation, an uncompensated Doppler rate is detrimental, especially for high values of the parameter SF . We thus proposed a receiver scheme that performs frame, timing, and frequency synchronization and also removes the Doppler rate effects. The performance achieved by this receiver is almost the same of an ideal AWGN channel, with small losses only for high values of SF.

This receiver has been used in a system simulator in [3]. It includes the interference coming from all the users in the field of view of the satellite, the frequency offsets due to the oscillators instability and computes the Doppler rate, the Doppler shift, and the attenuation for each transmitting user. To achieve better results it also makes use of interference cancellation after the successful detection of a packet.

Conclusions

In this thesis we analyzed three different scenarios of satellite communications and proposed optimized transceivers for them.

We first investigated a single-carrier per transponder scenario. We proposed three schemes for a cooperation among two receivers that communicate over a capacity constrained side-channel. We derived a closed form of an MMSE based receiver, that can also be extended to the CS framework. Then we proposed a receiver based on a modification of the BCJR to accommodate for the presence of the side-channel. Lastly, we tested a scheme that quantizes the LLRs instead of the symbols. We showed a comparison of their performance from an information rate perspective depending on the capacity of the constrained link. We also confirmed the correspondence among information rate results and packet error rate simulations with standard MODCODs.

The second scenario was focused on satellites for Earth observation. We considered two different configurations, when the satellite uses one or two separated radio-frequency chains, and applied several transceiver techniques. We saw that an optimization of the symbol rate can provide noticeable advantages with respect to the reference system. Moreover, for the two channels configuration, we have compared classical single-user detection, multiuser detection, and the Alamouti scheme. We also discussed on the introduction of an IC-CS receiver for high symbol-rate.

Finally, we studied a LEO satellite receiver to extend LoRa-based IoT networks. We first introduced the fundamental aspects of the LoRa protocol and modulation. We showed that the typical challenges of a LEO satellite scenario (i.e., Doppler shift and Doppler rate) have a huge impact on the performance of the LoRa modulation. Then, we proposed a receiver that could reliably receive LoRa signals in this scenario. It performs packet detection, frame synchronization, timing and frequency synchronization, and Doppler rate estimation and correction. Despite the number of impairments to take into account, we manage to reach a performance similar to that in an ideal AWGN channel, where the only impairment is noise.

Bibliography

[1] ETSI EN 302 307-2 Digital Video Broadcasting (DVB), Second generation framing structure, channel coding and modulation systems for Broadcasting, Interactive Services, News Gathering and other broadband satellite applications, Part II: S2-Extensions (DVB-S2X), Available on ETSI web site (http://www.etsi.org).

[2] O. B. A. Seller, et. al., “Low power long range transmitter,” 2014, EP Patent App. EP20,131,154,071.

[3] Y. Zanettini, “Techniques for interference mitigation in satellite communications,” Ph.D. dissertation, Università di Parma, 2017, PhD Thesis, University of Parma.

[4] T. M. Cover and J. A. Thomas, *Elements of Information Theory*, 2nd ed. New York: John Wiley & Sons, 2006.

[5] D. M. Arnold, H.-A. Loeliger, P. O. Vontobel, A. Kavčić, and W. Zeng, “Simulation-based computation of information rates for channels with memory,” *IEEE Trans. Inform. Theory*, vol. 52, no. 8, pp. 3498–3508, Aug. 2006.

[6] L. R. Bahl, J. Cocke, F. Jelinek, and J. Raviv, “Optimal decoding of linear codes for minimizing symbol error rate,” *IEEE Trans. Inform. Theory*, vol. 20, pp. 284–287, Mar. 1974.

[7] N. Merhav, G. Kaplan, A. Lapidoth, and S. Shamai, "On information rates for mismatched decoders," *IEEE Trans. Inform. Theory*, vol. 40, no. 6, pp. 1953–1967, Nov. 1994.

[8] U. Fincke and M. Pohst, "Improved methods for calculating vectors of short length in a lattice, including a complexity analysis," *Mathematics of computation*, vol. 44, no. 170, pp. 463–471, Apr. 1985.

[9] J. Hagenauer and C. Kuhn, "Turbo equalization for channels with high memory using a list-sequential (liss) equalizer," in *Proc. International Symposium on Turbo Codes and Related Topics (ISTC'03)*, 2003.

[10] K. K. Y. Wong, *The soft-output M-algorithm and its applications*. Queen's University, 2006.

[11] D. D. Falconer and F. Magee, "Adaptive channel memory truncation for maximum likelihood sequence estimation," *Bell System Tech. J.*, vol. 52, no. 9, pp. 1541–1562, Nov. 1973.

[12] F. Rusek and A. Prlja, "Optimal channel shortening for MIMO and ISI channels," *IEEE Trans. Wireless Commun.*, vol. 11, no. 2, pp. 810–818, Feb. 2012.

[13] S. Hu and F. Rusek, "On the design of channel shortening demodulators for iterative receivers in MIMO and ISI channels," available at *http://arxiv.org/abs/1506.07331*.

[14] ——, "On the design of reduced state demodulators with interference cancellation for iterative receivers," in *Proc. 24th IEEE Intern. Symp. on Personal, Indoor, and Mobile Radio Comm. (PIMRC)*, Hong Kong, China, Aug. 2015, pp. 981–985.

[15] A. Modenini, F. Rusek, and G. Colavolpe, "Adaptive rate-maximizing channel-shortening for ISI channels," *IEEE Commun. Letters*, vol. 19, no. 12, pp. 2090–2093, Dec. 2015.

[16] S. Haykin, *Adaptive Filter Theory*, 3rd ed. Englewood Cliffs, NJ: Prentice-Hall, 1996.

[17] A. Barbieri, D. Fertonani, and G. Colavolpe, "Improving the spectral efficiency of linear modulations through time-frequency packing," in *Proc. IEEE International Symposium on Information Theory*, Toronto, Canada, Jul. 2008, pp. 2742–2746.

[18] P. Banelli, S. Buzzi, G. Colavolpe, A. Modenini, F. Rusek, and A. Ugolini, "Modulation formats and waveforms for 5G networks: Who will be the heir of OFDM?" *IEEE Signal Processing Mag.*, vol. 31, no. 6, pp. 80–93, Nov. 2014.

[19] G. Colavolpe and T. Foggi, "Time-frequency packing for high capacity coherent optical links," *IEEE Trans. Commun.*, vol. 62, pp. 2986–2995, Aug. 2014.

[20] A. Modenini, G. Colavolpe, and N. Alagha, "How to significantly improve the spectral efficiency of linear modulations through time-frequency packing and advanced processing," in *Proc. IEEE Intern. Conf. Commun.*, Ottawa, Canada, Jun. 2012, pp. 3299–3304.

[21] S. Khattak, W. Rave, and G. Fettweis, "Distributed iterative multiuser detection through base station cooperation," *EURASIP Journal on Wireless Communications and Networking*, vol. 2008, no. 1, p. 390489, 2008. [Online]. Available: http://dx.doi.org/10.1155/2008/390489

[22] ETSI EN 302 307-1 Digital Video Broadcasting (DVB), Second generation framing structure, channel coding and modulation systems for Broadcasting, Interactive Services, News Gathering and other broadband satellite applications, Part I: DVB-S2, Available on ETSI web site (http://www.etsi.org).

[23] S. Cioni, G. Colavolpe, V. Mignone, A. Modenini, A. Morello, M. Ricciulli, A. Ugolini, and Y. Zanettini, "Transmission parameters optimization and receiver architectures for DVB-S2X systems," *International Journal of Satellite Communications and Networking*, vol. 34, pp. 337–350, May/June 2016, article first published online: June 2015.

[24] A. Ugolini, A. Modenini, G. Colavolpe, V. Mignone, and A. Morello, "Advanced techniques for spectrally efficient DVB-S2X systems," *International Journal of Satellite Communications and Networking*, vol. 34, pp. 609–623, Sep./Oct. 2016, article first published online: September 2015.

[25] H. Meyr, M. Oerder, and A. Polydoros, "On sampling rate, analog prefiltering, and sufficient statistics for digital receivers," *IEEE Trans. Commun.*, vol. 42, pp. 3208–3214, Dec. 1994.

[26] G. Karam and H. Sari, "Analysis of predistortion, equalization, and ISI cancellation techniques in digital radio systems with nonlinear transmit amplifiers," *IEEE Trans. Commun.*, vol. 37, pp. 1245–1253, Dec 1989.

[27] E. Casini, R. De Gaudenzi, and A. Ginesi, "DVB-S2 modem algorithms design and performance over typical satellite channels," *Intern. J. of Satellite Communications and Networking*, vol. 22, no. 3, pp. 281–318, May/June 2004.

[28] V. Kostina and S. Verdú, "Nonasymptotic noisy lossy source coding," *IEEE Transactions on Information Theory*, vol. 62, no. 11, pp. 6111–6123, Nov 2016.

[29] J. M. Cioffi, G. P. Dudevoir, M. V. Eyuboglu, and G. D. Forney, "MMSE decision-feedback equalizers and coding. I. Equalization results," *IEEE Trans. Commun.*, vol. 43, no. 10, pp. 2582–2594, Oct 1995.

[30] G. D. Forney, Jr., "Maximum-likelihood sequence estimation of digital sequences in the presence of intersymbol interference," *IEEE Trans. Inform. Theory*, vol. 18, pp. 284–287, May 1972.

[31] G. Ungerboeck, "Adaptive maximum likelihood receiver for carrier-modulated data-transmission systems," *IEEE Trans. Commun.*, vol. com-22, pp. 624–636, May 1974.

[32] S. Cioni, G. Colavolpe, C. Ernst, and A. Ginesi, "Bandwidth optimization for satellite digital broadcasting," in *31st AIAA International Communications Satellite Systems Conference*, Florence, Italy, Oct. 2013.

[33] A. Ganti, A. Lapidoth, and I. E. Telatar, "Mismatched decoding revisited: General alphabets, channels with memory, and the wide-band limit," *IEEE Trans. Inform. Theory*, vol. 46, no. 7, pp. 2315–2328, Nov. 2000.

[34] G. Caire, G. Taricco, and E. Biglieri, "Bit-interleaved coded modulation," *IEEE Trans. Inform. Theory*, vol. 44, no. 3, pp. 927–946, May 1999.

[35] L. Ding, G. Zhou, D. Morgan, M. Zhengxiang, J. Kenney, K. Jaehyeong, and C. Giardina, "A robust digital baseband predistorter constructed using memory polynomials," *IEEE Trans. on Commun.*, vol. 52, no. 1, pp. 159–165, Jan. 2004.

[36] N. Mazzali, B. Shankar, and B. Ottersten, "On-board signal predistortion for digital transparent satellites," in *Proc. IEEE Intern. Work. on Signal Processing Advances for Wireless Commun.*, Stockholm, Sweden, June-July 2015, pp. 535–539.

[37] N. Kelly, M. Allegue-Martínez, P.-D. Arapoglou, and A. Zhu, "Bandwidth-constrained digital pre-compensation technique for multi-carrier satellite communications," *International Journal of Satellite Communications and Networking*, vol. 34, pp. 171–194, March/April 2016, article first published online: April 2015.

[38] CCSDS 131.2-B-1, Flexible advanced coding and modulation scheme for high rate telemetry applications, Mar. 2012, Available at http://public.ccsds.org/publications/BlueBooks.aspx.

[39] W. Cauer, *Synthesis of linear communication networks*, 2nd ed. New York: McGraw–Hill, 1958.

[40] J. E. Mazo, "Faster-than-Nyquist signaling," *Bell System Tech. J.*, vol. 54, pp. 1450–1462, Oct. 1975.

[41] J. E. Mazo and H. J. Landau, "On the minimum distance problem for faster-than-Nyquist signaling," *IEEE Trans. Inform. Theory*, pp. 1420–1427, Nov. 1988.

[42] A. Liveris and C. N. Georghiades, "Exploiting faster-than-Nyquist signaling," *IEEE Trans. Commun.*, vol. 47, pp. 1502–1511, Sep. 2003.

[43] F. Rusek and J. B. Anderson, "The two dimensional Mazo limit," in *Proc. IEEE International Symposium on Information Theory*, Adelaide, Australia, Nov. 2005, pp. 970–974.

[44] A. Barbieri, D. Fertonani, and G. Colavolpe, "Time-frequency packing for linear modulations: spectral efficiency and practical detection schemes," *IEEE Trans. Commun.*, vol. 57, pp. 2951–2959, Oct. 2009.

[45] A. Piemontese, A. Modenini, G. Colavolpe, and N. Alagha, "Improving the spectral efficiency of nonlinear satellite systems through time-frequency packing and advanced processing," *IEEE Trans. Commun.*, vol. 61, no. 8, pp. 3404–3412, Aug. 2013.

[46] S. Verdú, *Multiuser Detection*. Cambridge, UK: Cambridge University Press, 1998.

[47] S. M. Alamouti, "A simple transmit diversity technique for wireless communications," *IEEE J. Select. Areas Commun.*, vol. 16, no. 8, pp. 1451–1458, Oct. 1998.

[48] A. Modenini, A. Ugolini, A. Piemontese, and G. Colavolpe, "On the use of multiple satellites to improve the spectral efficiency of broadcast transmissions," *IEEE Trans. Broadcast.*, vol. 61, no. 4, pp. 590–602, Dec. 2015.

[49] M. J. D. Powell, "The BOBYQA algorithm for bound constrained optimization without derivatives," Department of Applied Mathematics and Theoretical Physics, Cambridge, England, Tech. Rep., Aug. 2009.

[50] S. G. Johnson, "The NLopt nonlinear-optimization package," *http://ab-initio.mit.edu/nlopt*.

[51] G. Colavolpe, A. Modenini, A. Piemontese, and A. Ugolini, "Multiuser detection in multibeam satellite systems: Theoretical analysis and practical schemes,"

in *Proc. IEEE Intern. Work. on Signal Processing Advances for Wireless Commun.*, Stockholm, Sweden, June-July 2015, pp. 525–529.

[52] M. Witzke, S. Baro, F. Schreckenbach, and J. Hagenauer, "Iterative detection of mimo signals with linear detectors," in *Conference Record of the Thirty-Sixth Asilomar Conference on Signals, Systems and Computers, 2002.*, vol. 1, Nov 2002, pp. 289–293 vol.1.

[53] C. Studer, S. Fateh, and D. Seethaler, "Asic implementation of soft-input soft-output mimo detection using mmse parallel interference cancellation," *IEEE Journal of Solid-State Circuits*, vol. 46, no. 7, pp. 1754–1765, July 2011.

[54] J. Zhang, H. Nguyen, and G. Mandyam, "Lmmse-based iterative and turbo equalization methods for cdma downlink channels," in *IEEE 6th Workshop on Signal Processing Advances in Wireless Communications, 2005.*, June 2005, pp. 231–235.

[55] LoRa Alliance, Inc., "LoRaWAN Specification," Jul. 2016.

[56] S. G. Wilson, *Digital Modulation and Coding*. Prentice Hall, 1996.

[57] I. S. Gradshtein and I. M. Ryzhik, *Table of Integrals, Series and Products*. New York: Academic Press, 1980.

[58] A. Papoulis, *Probability, Random Variables and Stochastic Processes*. New York, NY: McGraw-Hill, 1991.

[59] S. Benedetto and E. Biglieri, *Principles of Digital Transmission: With Wireless Applications*. Norwell, MA, USA: Kluwer Academic Publishers, 1999.

[60] G. Colavolpe and R. Raheli, "Theoretical analysis and performance limits of noncoherent sequence detection of coded PSK," *IEEE Trans. Inform. Theory*, vol. 46, no. 4, pp. 1483–1494, Jul. 2000.

[61] D. C. Rife and R. R. Boorstyn, "Single tone parameter estimation from discrete-time observations," *IEEE Trans. Inform. Theory*, vol. 20, pp. 591–598, September 1974.

[62] U. Mengali and M. Morelli, "Data-aided frequency estimation for burst digital transmission," *IEEE Trans. Commun.*, vol. 45, pp. 23–25, Jan. 1997.

[63] A. N. D'Andrea, U. Mengali, and R. Reggiannini, "The modified Cramer-Rao bound and its application to synchronization problems," *IEEE Trans. Commun.*, vol. 42, pp. 1391–1399, Feb. 1994.

[64] I. Ali, N. Al-Dhahir, and J. E. Hershey, "Doppler characterization for LEO satellites," *IEEE Trans. Commun.*, vol. 46, pp. 309–313, Mar. 1998.

[65] M. Morelli, "Doppler-rate estimation for burst digital transmission," *IEEE Trans. Commun.*, vol. 50, pp. 707–710, May 2002.

Acknowledgements

The list of people that helped me during the last three years is fairly long and I am hoping I am not forgetting anyone. The first person to thank is my tutor, Giulio. Firstly, because he believed in me and took me in his research group. But also for the help, the insightful discussions, the guidance throughout the PhD and the huge amount of patience. Then, it is natural to thank the whole SpadicLab. Alessandro, Andrea (for a short period), Tommy and Yuri have been the best team one could think of. They helped me anytime I asked for advice, and taught me a lot. Really a lot! Yuri deserves a special "thank you", since he started this adventure with me and we spent three years in the same office: needless to say, we also shared a lot of laughs, a lot of work, a lot of food and a lot of coffees. Thanks for all the suggestions, the help you gave me and all the "*Michelangelo, ti sei ricordato di consegnare i documenti in segreteria?*". (And thanks of course for the best memes on Whatsapp!)

Talking about coffee, I need to thank Matteo and Simone, for all the coffees, the matched-betting and especially for their "fair" monetary loans.

It is time to move abroad now. During my experience in Lund University, Sweden, I met a group of very nice and smart people that made me feel welcome from the very beginning. I quickly became part of the group and had the impression that not only we were “on the same wavelength”, but we were probably also using the same modulation scheme. First I want to thank Fredrik for his advice, for his time and for accepting the burden of my presence in Lund University. In only two months he taught me a lot about information theory, telecommunications and Swedish culture. Then, I thank Dimitrios, Muris, João and Zach for their friendliness, for the beers, the fika and the insightful discussions about life at Medicon and Rosegarden. I also want to thank Husha for his kindness and helpfulness.

Of course, I cannot forget to thank my closest friends and my brothers (there’s no need to make a list, they know who they are). Their company and the laughs I shared with them are among the things that gave me strength and joy even in the darkest moments. It’s not a coincidence I put friends and brothers in the same paragraph.

Grazie a mia madre e a mio padre. Per il loro supporto e per tutto ciò che mi hanno insegnato. Non sarei arrivato nè a questa, nè alle altre tesi senza la loro guida.

Last but not least, thanks Valeria. Thanks for the patience you showed and everything you did for me. I could write a list of the reasons, but it would be longer than the thesis itself. And it would probably not be sufficient, anyway.

Michelangelo